catalysts

MDPI

Review

Insights into the Recent Progress and Advanced Materials for Photocatalytic Nitrogen Fixation for Ammonia (NH_3) Production

Manh-Hiep Vu [1], M. Sakar [1,2] and Trong-On Do [1,*]

[1] Department of Chemical Engineering, Laval University, Québec, QC G1V 0A6, Canada; manh-hiep.vu.1@ulaval.ca (M.-H.V.); sakar.mohan.1@ulaval.ca (M.S.)
[2] Centre for Nano and Material Sciences, Jain University, Bangalore 562 112, India
* Correspondence: trong-on.do@gch.ulaval.ca; Tel.: +1-(418) 656-3774

Received: 20 November 2018; Accepted: 30 November 2018; Published: 4 December 2018

Abstract: Ammonia (NH_3) is one of the key agricultural fertilizers and to date, industries are using the conventional Haber-Bosh process for the synthesis of NH_3 which requires high temperature and energy. To overcome such challenges and to find a sustainable alternative process, researchers are focusing on the photocatalytic nitrogen fixation process. Recently, the effective utilization of sunlight has been proposed via photocatalytic water splitting for producing green energy resource, hydrogen. Inspired by this phenomenon, the production of ammonia via nitrogen, water and sunlight has been attracted many efforts. Photocatalytic N_2 fixation presents a green and sustainable ammonia synthesis pathway. Currently, the strategies for development of efficient photocatalyst for nitrogen fixation is primarily concentrated on creating active sites or loading transition metal to facilitate the charge separation and weaken the N–N triple bond. In this investigation, we review the literature knowledge about the photocatalysis phenomena and the most recent developments on the semiconductor nanocomposites for nitrogen fixation, following by a detailed discussion of each type of mechanism.

Keywords: photocatalysis; ammonia synthesis; N_2 fixation; Haber-Bosch process

1. Introduction

In this current century, the climate changes and energy production are some of the most significant and important challenges that are being faced by the people in the world. In this direction, ammonia (NH_3) and the associated chemicals could provide an alternative energy resource. Similar to molecular hydrogen (H_2), NH_3 is also a carbon-free energy-source for the end-users. Ammonia has a worldwide annual production of around 150 million tons, due to the increasing demand from an increasing world population. However, the depletion of fossil fuels makes the industrial-scale ammonia synthesis processes urges to replace the usages of fossil fuels by a renewable energy source. Currently, NH_3 is being manufactured by the traditional Haber-Bosch (HB) process using pure H_2 and N_2, which requires energy-intensive high temperature (>500 °C) and extremely high pressure (200–300 bar). Nevertheless, the utilization of natural gas as a source of H_2 obtained by steam/gas reforming into the production of ammonia takes up about 1–2% world energy every year and belches out hundreds of millions of tons of CO_2 annually [1,2].

Specifically, in Canada, there are 11 plants manufacturing NH_3 across the country, where they use this HB process to produce ~5 million tons of NH_3 every year. Canada provides approximately 12% of the world's fertilizer-materials and ~25% of the ammonia produced in Canada is being sent to North America for its direct use the agricultural purposes. The fertilizer industry creates ~$12 billion

in annual economic activity in Canada. Therefore, it is of a considerable significance to develop the low-energy consumption, sustainable and eco-friendly process to manufacture NH_3 through nitrogen fixation in large scale.

This review sheds lights into the recent progress in the development of a variety of routes for the synthesis of advanced materials and emphasizes their application for nitrogen photofixation. This review also concludes with a concise overview of the present status, analyzes potential and future development of photocatalysts with a view towards enhanced performance in different photocatalytic materials.

2. A Brief Insight into the Haber-Bosch Process

The most industrial and practical process for ammonia production is the Haber-Bosch process, where ammonia (NH_3) is produced directly from its constituent elements, such as hydrogen (H_2) and nitrogen (N_2). Conventionally, this synthesis is conducted at 150–250 atm and 400–500 °C, as the gas passes over the reactor with two or four beds of catalyst (Figure 1). Eventually, each time conversion to ammonia is only 15%, by multiple times recycle unreacted gases, an overall conversion of 97% is obtained. The primary source of molecular H_2 is methane from the natural gas. In addition, it is estimated that around 3–5% of the world's natural-gas production is utilized in the Haber-Bosch (HB) process.

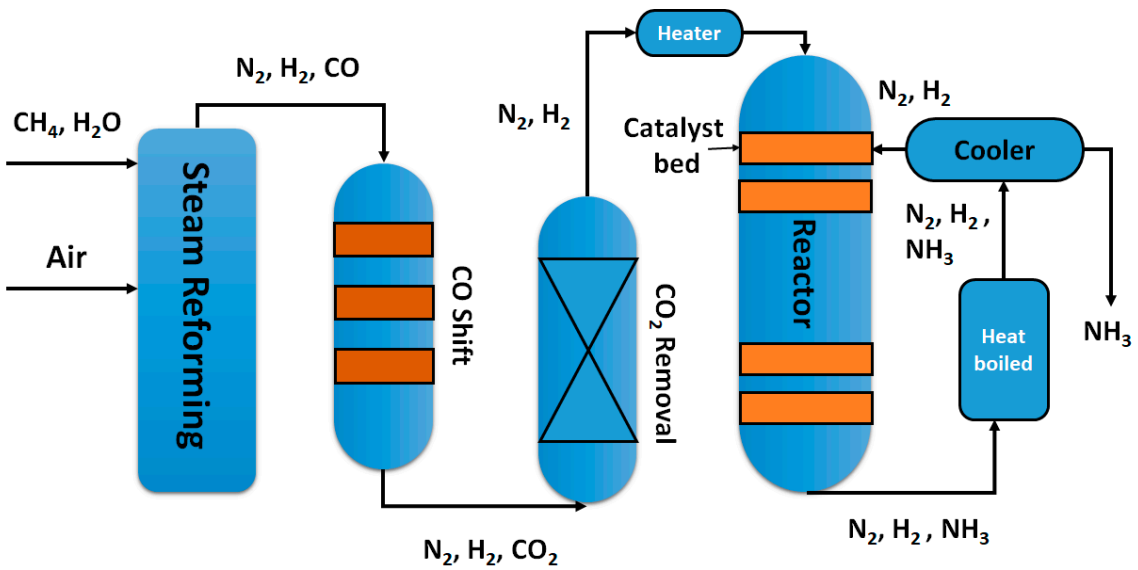

Figure 1. A flow scheme for the Haber-Bosch process.

2.1. Equilibrium Considerations and Reaction Rate

In the Haber-Bosch process, the formation reaction of NH_3 is reversible and the forward reaction of NH_3 production is an exothermic: $N_{2(g)} + 3H_{2(g)} \rightarrow 2NH_{3(g)}$ ($H = -92$ kJmol^{-1}). According to Le Chatelier's principle, this reaction will be supported at the lower temperatures. In this process, the temperature must be as low as possible towards getting as much as ammonia as possible in the equilibrium condition. However, under this condition, the reaction does not proceed at an efficient rate. Therefore, two contrasting considerations are occurring in this synthesis. The viable temperature for this process is 400–450 °C, which bound to produce a reasonably high amount of NH_3 in the equilibrium mixture (15%) in a very short time.

2.2. Catalyst and Mechanism

The most common catalyst of the Haber-Bosch process based on K_2O or Al_2O_3-promoted iron catalyst. The mechanism that involves the heterogeneous-catalyst is proposed to have the following steps:

$$N_{2(g)} \rightarrow N_{2(adsorbed)} \quad (1)$$

$$N_{2(adsorbed)} \rightarrow 2N_{(adsorbed)} \quad (2)$$

$$H_{2(g)} \rightarrow H_{2(adsorbed)} \quad (3)$$

$$H_{2(adsorbed)} \rightarrow 2H_{(adsorbed)} \quad (4)$$

$$N_{(adsorbed)} + 3H_{(adsorbed)} \rightarrow NH_{3(adsorbed)} \quad (5)$$

$$NH_{3(adsorbed)} \rightarrow NH_{3(g)} \quad (6)$$

Reaction (5) occurs in three steps, forming the NH, NH_2 and finally NH_3. The experimental evidence to Reaction (2) as being the slow, rate-determining step. This is expected since the nitrogen triple bond is the strongest of the bonds that must be broken.

2.3. Separation of the Ammonia

When the produced NH_3 gases depart from the reactor, they are essentially hot and under a very high pressure. However, ammonia will be easily liquefied under such pressure as long as it is not too hot and therefore the temperature of the mixture will be sufficiently lowered for the ammonia gas to turn into a liquid. Notably, the molecular N_2 and H_2 remain as gaseous states under these high pressures and they can be recycled.

3. Overview: Fundamental of Photocatalytic Nitrogen Fixation

3.1. The Principle of Photocatalysis on Semiconductors

Semiconductors (SCs) are used as photocatalytic materials, thanks to their suitable amalgamation of electronic properties, structure, light-absorption characteristics, charge transport dynamics and favorable lifetime of their excited-state charge carriers. Basically, an SC possesses an energy gap between the top of the filled-valence band (VB) and the bottom of the vacant-conduction band (CB), which is known as the band gap energy of the SC [3–6]. Thus, the separation of charge carrier between these bands only occurs with sufficient energy supply. In semiconductors, the photocatalytic process involves three main steps: Light absorption, charge separation and catalytic reaction. Under light illumination, the electron absorbs a photon with energy higher than or equal to the band gap energy of the semiconductor, excites from VB to CB and releases hole in the VB (Figure 2). This light-induced promoting electron-hole separation is a prerequisite step in all semiconductor photocatalysis. Finally, the photo-generated species transfer to the semiconductor surface and initiate redox reaction of absorbed reagents. However, electrons and holes are to recombine and dissipate the energy in the bulk (volume) or on the surface of the semiconductor, because of the kinetic-barrier for the electron-hole recombination process is relatively low, resulting in a decrease of reaction efficiency [7]. Therefore, prevention of charge recombination is a significant challenge in the photocatalytic field. In the last decades, there has been a considerable amount of effort to increase the lifetime of photogenerated carriers, such as developing photocatalyst with the nanostructure, co-catalyst, surface engineering and junction [8,9].

Moreover, a wide variety of semiconductors, mainly metal oxide and chalcogenides, have been examined with capability for photocatalyst, but only a few of them are considered to be effective photocatalyst, because of the appreciable band gap. In general, wide-band gap semiconductors prove to be better photocatalytic activity compared with low-band gap catalysts. For example, titanium dioxide showed better photocatalysis than cadmium sulfide for hydrogen production, due to the

increased free energy of photo-induced charge species of the TiO_2 and the intrinsic low chemical- and photo-chemical stability of the CdS. However, the narrow-band gap materials (such as metal sulfides) absorb solar light better that pave the way to potentially use the effective natural light source, which is the sunlight. Accordingly, a promising strategy with this concern has been attained with the utilization of several methods aiming to improve the electronic state and optical characteristics of semiconductors, including metal deposition, doping, and dye-sensitization. On the other hand, to obtain the effective photocatalytic procedure, the bottom of the CB must be located at a more negative potential than the reduction potential of electron acceptor (A) while the top of CB must beyond the oxidation-potential of electron-donor (D).

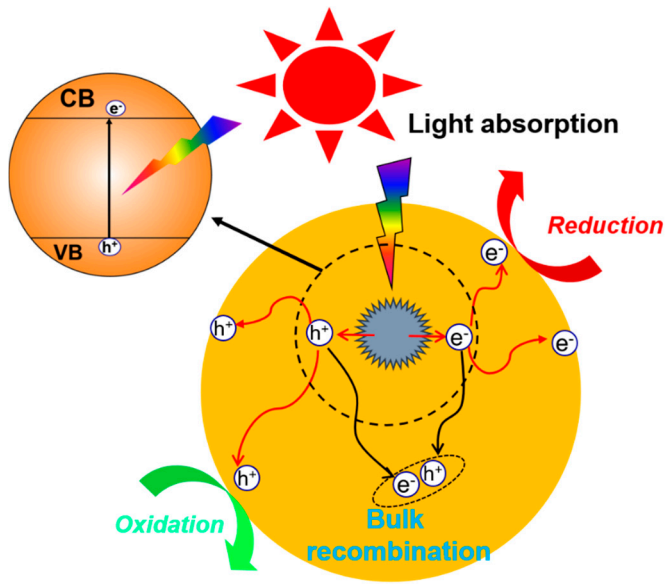

Figure 2. Simulation of semiconductor photocatalysis under light irradiation.

3.2. Quantum Yield (QY)

The efficiency of the photocatalytic process is measured by quantum yield (QY), which has been considered to describe the number of molecules converted relative to the total number of incident-photons on the reactor walls for an unknown reactor-geometry and for a polychromatic radiation.

$$\mathrm{QY}(\Phi) = \frac{\#\ \text{molecule decomposed}}{\#\ \text{photon absorbed}}$$

Additionally, quantum yield could be calculated based on the rate of reaction dividing to the absorbed light intensity (I_a),

$$\Phi = \frac{\text{Rate}}{\text{Ia}}.$$

The measurement of the absorbed light intensity is easy in homogeneous systems; however, it is difficult for heterogeneous reactions, such as thin films or semiconductor suspensions. In this stage, the suspended particle also reflected and scattered incident light instead of total absorption. Thus, it is very exhausted to correct this loss, including 13–76% of the total incident photon flux [10]. Otherwise, light is also absorbed by products or educts of reaction, suggesting QY should be determined at very early reaction time. To conquer such problems in heterogeneous photoreaction, it was proposed replacing the absorbed light intensity by the incident intensity (I_0). Therefore, apparent quantum yield (AQY, ς) [11,12] has been termed to measure the efficiency of the photocatalytic process:

$$\varsigma = \frac{\text{Rate}}{I_0}.$$

3.3. Materials for Photocatalysis

Based on fundamental chemical composition system, all of the semiconducting materials can be divided into three important categories, mainly metal oxides, metal sulfides and metal free semiconductors.

Usually, metal oxides are the most common material, which can be utilized for photocatalysis in various reactions, such as H_2 production, CO_2 reduction and N_2 fixation. This type of materials have a wide range of applications according to their band structure and activities. However, most of them only activate under UV light irradiation due to their large band gap energy. To overcome this difficulty, the substitutions of cations or anions in the lattice of a wide band gap semiconductor has been employed to narrow band gap energy, enhancing the visible light respond. This substitution of cations and anions in the crystal lattice may form intermediate energy levels (due to the energy levels of impurities) within the band gap of photocatalyst that facilitates their absorption in the visible range. For example, titanium dioxide with the properties of stability, non-toxicity and high photocatalytic activity is potentially a suitable catalyst for water splitting reaction. Nevertheless, it only absorbs UV light due to a wide band gap (Eg = 3.2 eV). To deal with this disadvantage, Khan et al. modified n-type TiO_2 chemically by doping C on this material. Carbon replaces some of the lattice oxygen atoms, resulting in a decrease in band gap energy to 2.32 eV [13].

Contrary to metal oxides, the metal sulfides normally possess a narrow band gap. Thus, they can absorb visible light to generate electron-hole. Moreover, the conduction reduction potential of water is less negative than their CB and so they can reduce water into molecular hydrogen. Otherwise, these materials also have several disadvantages, such as instability and fast recombination of photoexcited charges. The most common example is cadmium sulfide, one of the best semiconductors with high activity for hydrogen production under visible light illumination. With narrow band gap materials, the recombination process of electron and hole is very easy. Reducing particle size of CdS can provide more active sites, decrease the travel path of migration of photoexcited electron to the semiconductor surface and prevent charge recombination [14]. In addition, combining CdS nanoparticles with other semiconductors can also enhance their stability and photocatalytic activity [15–18].

Beside these semiconductors, some nitride-based systems also exhibit photocatalytic activities towards water reduction in the visible range of solar light. Recently, graphitic carbon nitride (g-C_3N_4) has drawn a lot of attention, because of its intrinsic properties, such as narrow band gap and non-toxicity. This metal-free polymeric material shows hydrogen evolution under visible light illumination with high chemical stability. Nevertheless, its photo-conversion efficiency is considerably limited than that of TiO_2 or CdS and therefore it requires further efforts to improve its photocatalytic activities.

3.4. Co-Catalyst Loading

A Cocatalyst is an integrated compound to the semiconducting material to promote their photocatalytic activity. In a water decomposition reaction, the cocatalyst can avail enhancing either water reduction or oxidation half reaction. In photocatalysis, cocatalysts are typically tiny metal nanoparticles (NPs), which create a Schottky junction with semiconductor and support for charge-separation in a photocatalyst of a photochemical cell [19,20]. In principle, the interfacial-contact between the semiconductor and metal induces an electric field, which effectively separates the excited electrons and holes more easily [21–23]. Additionally, the metal supplies active sites for H_2 generation due to its comparatively low over the water reduction potential.

The most common cocatalysts for photocatalysis are Pt, Rh, Au, NiO, and RuO_2. Maeda et al. report that loading both Rh/Cr_2O_3 and Mn_2O_3 supported on GaN:ZnO can effectively promote overall water splitting under visible light although the quantum yield of this system was relatively low [24]. Maeda proved that Rh/Cr_2O_3 acted as electron collectors to host hydrogen evolution while the main function of is the active sites for water oxidation reaction. However,

almost of cocatalyst are noble metals which are rare and expensive, thus prohibiting their wide scale application. Therefore, the development of non-noble and low-cost cocatalyst is extremely important. The physical and chemical characteristics of the co-catalyst, such as particle size and valence states directly affect their activity and are strongly dependent on their loading method onto the surface of host SCs. Although depositing more co-catalyst (concentration) provides more active sites for photocatalytic reactions, it considerably reduces the absorption ability of the semiconductor photocatalyst. Thus, the concentration or the loading amount of co-catalyst should be controlled and optimized to achieve the maximum activity.

3.5. Localized Surface Plasmon Resonance in Photocatalysis

Localized surface plasmon resonance (LSPR) labels the collective charge carrier oscillations in metal nanoparticle created by an incident field that resonant with the periodic movement of the negative charge against the positive nuclei background [25]. In general, the LSPR appears when the size of the metal nanoparticle is considerably smaller than the wavelength of incident light. Upon resonance irradiation, the charge oscillations induce a large electric dipole at the same frequency as that of the incident electric field. Consequently, the electric field intensity in the vicinity of plasmonic metal nanoparticles strengthens up to 1000 times as high as that of the incident field and greatly increases far-field scattering. In a plasmonic-heterostructure, the stored energy in the LSPR can be (i) transferred to the semiconductor or (ii) re-emitted as scattered photons (Figure 3A).

LSPR effect can be effectively applied in photocatalysis by the non-radiative transfer process. Under visible light excitation, LSPR generates hot electrons in the plasmonic nanostructured metal. It should be noted that these electrons possess higher energies than the level of thermal excitation. The injection of the hot electrons into a semiconductor improves the solar photo-voltaic energy conversion. Additionally, the existence of a Schottky barrier at the junction between the metal/semiconductor systems can block electron migration. If the hot electrons absorb sufficient photon energy, they can overcome the barrier and transfer into the conduction band of semiconductor (Figure 3B). Interestingly, the charge carrier injections can occur either from semiconductor or plasmonic metal. It is likely that the excitation state of the semiconductor and plasmonic metal decide where the charge carriers are injected.

The solar energy conversion efficiency can be improved by plasmonic nanocomposites via the two possible following mechanisms: (1) Direct electron transfer (DET) or by (2) plasmon induced resonant energy transfer (PIRET) [26]. The enhancement of the light absorption in semiconductors by photonic enhancement via (i) increasing the length of the optical path and (ii) concentrating the incident field than that of directly transferring the plasmonic energy from the metal to the semiconductor to induce the charge separation in the semiconductor. The plasmonic charge (hot electron) transfer process is referred to as direct electron transfer, which requires the semiconductor and the plasmonic metal be in direct contact with each other (Figure 3C). However, DET differs in that the plasmonic metal does not have a band gap to determines the charge-transfer kinetics [27]. Rather, the plasmonic carriers have the energy that proportional to the incident photon's energy besides the Fermi level, therefore they can easily overcome the barriers that are energetically unfavorable at the interface, leading to more choices in the selection of materials. As another mode of non-radiative process, the PIRET is an attractive phenomenon for plasmonic enhancement (Figure 3D).

PIRET describes the non-radiative transfer of energy from the metal LSPR dipole to the semiconductor transition dipole. PIRET depends on the spectral overlap and it does not require any electronic-alignment or even physical-contact to transfer energy as like in DET [29], which essentially provides flexibility in the design of solar energy materials and structures. PIRET can produce electron-hole pairs in the semiconductors, suggesting a strong coupling to the weak band edge states. The plasmon resonance can easily be tuned, which allows for an enhanced solar energy harvesting in the entire visible spectrum. PIRET is also favorable when the charge transfer process creates undesirable effects, such as the degradation of materials or issues in the carrier equilibration.

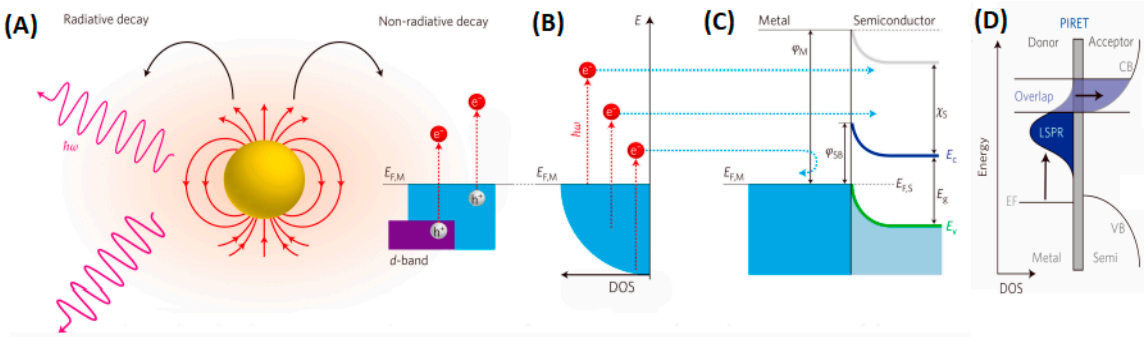

Figure 3. (**A**) High-energy resonant state decay in two possible form: Re-emission of photons or the generation of energetic charge carriers; (**B**) excitation electron from occupied energy level to a level above the Fermi energy; (**C**) hot electron overcoming the Schottky barrier and injected to the conduction band of the neighboring semiconductor; (**D**) plasmon-induce resonance energy transfer. (Reproduced with permission from MDPI [28]).

3.6. Fundamentals of Photocatalytic Nitrogen Fixation Principle

Since the first work reported by Fujishima and Honda, in the early 1970s, the use of photocatalysts, based on semiconductors, has emerged as the most promising and practical solution to address the challenges of energy and environmental issues [30]. In the last few decades, a renewed interest has been devoted in photocatalytic NH_3 production, and several papers have illustrated ammonia [31] and nitrate formation [32] using various kinds of semiconducting photocatalysts, plasmon-enhanced systems, and biomimetic systems.

Basically, the photocatalytic process of N_2 fixation is divided into several steps as follows: First, under the sunlight irradiation, photo-generated electrons are excited to the CB, leaving holes in the VB. Afterwards, some of the electrons and holes recombine together, meanwhile, other photo-formed holes (h^+) oxidize the water into H^+, and O_2 (Equation (7)) and N_2 reduction by hot-electrons lead to the production of NH_3 (Equation (8)). As a result, NH_3 is synthesized from water and N_2 under ambient conditions using the sunlight as an energy source (Equation (9)). Figure 4 demonstrates the scheme process of photocatalyst materials using for the reduction of nitrogen to ammonia.

$$2H_2O + 4h^+ \rightarrow O_2 + 4H^+ \tag{7}$$

$$N_2 + 6H^+ + 6e^- \rightarrow 2NH_3 \tag{8}$$

$$\frac{1}{2}N_2 + 3/2H_2O \rightarrow NH_3 + \frac{3}{4}O_2 \tag{9}$$

Although the proposed photocatalytic fixing nitrogen pathway is acceptable, many pending questions regarding the mechanisms, rates, and thermodynamics still remain. The protonation reactions versus standard potential are summarized by Lyndley et al. (Table 1). Thermodynamically, ammonia formation is favored, with an energy difference of 0.43 V between NH_3 and N_2H_4 and a 1.26 V between NH_3 and N_2H_2. In a thermodynamic aspect, the half-reaction generated NH_3 is capable of any photocatalyst semiconductor possessing a bandgap energy larger than 1.2 eV with proper conduction and valence band position. However, this half reaction involves multiple-electron transfer (6 electrons) and thus may be more kinetically challenging. Another limitation is the absorption of N_2 molecules over semiconductor photocatalysts and cleavage of highly stable N-N triple bond in order to activate dinitrogen. To overcome these challenges, it is necessary to create appropriate active sites that can effectively absorb nitrogen. This active site also serves as a trapping cage to capture electrons then transfer to absorbed nitrogen as well as suppress charge carrier recombination.

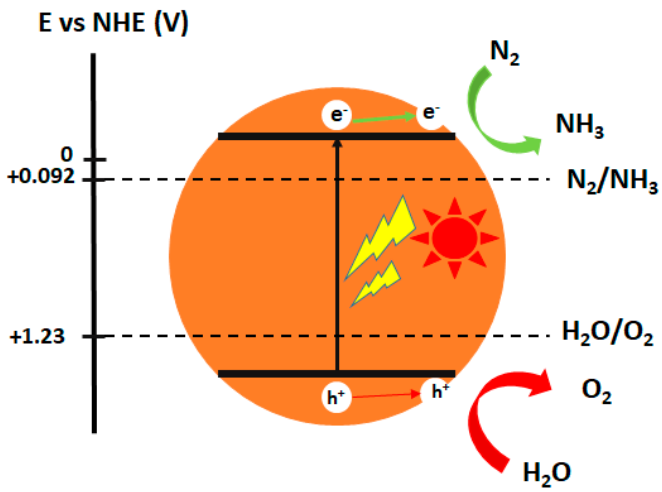

Figure 4. Schematic of semiconductor-based photocatalyst used for the N_2 fixation. The redox potentials (Potential (E) vs. Normal Hydrogen Electrode (NHE)) of half reaction water oxidation and dinitrogen protonation are marked on the left.

Table 1. Reduction potentials (vs. Standard Hydrogen Electrode (SHE)) of typical hydrogenation reactions relate to the reduction of N_2 to NH_3.

Reaction	E° (V) vs. SHE
$N_2 + 2H^+ + 2e^- \rightleftharpoons N_2H_2$	+0.035
$N_2 + 4H^+ + 4e^- \rightleftharpoons N_2H_4$	−0.4
$N_2 + 6H^+ + 6e^- \rightleftharpoons 2NH_3$	−1.22

4. Classification of Photocatalysts for N_2 Fixation Based on Active Sites

4.1. Metal Active Sites

4.1.1. Iron Active Sites

It should be noted that the catalyst of iron is the common catalyst in the Haber-Bosch process due to its good interaction with dinitrogen and weakening N–N bond [33]. In fact, recent studies indicate that ferric photocatalyst is capable of nitrogen reduction to ammonia. However, it is well-known that pure iron oxide had no activity in N_2 photofixation. To overcome this bottleneck, several researchers have employed a various method in the synthesis of defect iron catalyst. Tennakone [34] and his co-worker reported the first system of N_2 reduction using amorphous $Fe_2O_3 \cdot nH_2O$ under visible light irradiation. Fe_2O_3 was prepared by gradual addition of KOH to $FeCl_3$ solution and purged with N_2. After irradiated visible light for 40 min, a maximum ammonia concentration of ca. 4 μmol·L^{-1} was obtained and continuously decreased due to the decomposition of NH_3 to nitrate in the solution, which poisoned the catalyst. Therefore, NH_3 must be removed immediately from the reaction site to maintain catalytic efficiency. Khader et al. successfully prepared a mixture of α-Fe_2O_3 and Fe_3O_4, which was effective in photo-reduction of nitrogen for about 580 h [35]. Interestingly, in the existence of 5 at% iron in the form of Fe^{2+} in the partially reduced Fe_2O_3, NH_3 was detected in an aqueous slurry of the catalyst under UV illumination.

On the other hands, doping Fe into metal oxide, such as TiO_2, Al_2O_3, ZnO, is a practical strategy for utilization of iron active site catalysts. Most of the studies have been focused on metallic Fe modified titanium dioxide photocatalyst. In addition, there has been considerable debate over the role of cation Fe on iron titania photocatalyst. The earlier work suggested that the introduction of Fe^{3+} as an impurity in titania can play an indirect role in decreasing bandgap energy of semiconductor as well as hinders the recombination of photo-generated electron-hole pairs, consequently enhance the absorption ability and the photoactivity. Zhao et al. investigated the photocatalytic activity of Fe-doped TiO_2 with highly

exposed (101) facets [36]. The quantum yield of nitrogen photo-reduction using ethanol as scavenger can be reached to 18.27 × 10^{-2} m^{-2}. The transmission electron microscopy (TEM) images confirmed that Fe^{3+} ions are successfully incorporated into the anatase crystal and substituted for Ti^{4+} in the TiO_2 lattice (Figure 5). Zhao and Soria [37] reported that even doping Fe^{3+} can improve catalytic activity higher than pristine TiO_2, but an excess amount of Fe^{3+} doping can limit the continuous growth of TiO_2 particles and poisoning the catalyst. In a continuous work of previous studies, further investigations of mechanism on iron titanate photocatalyst were conducted by Rusina [38] and Krich [39] The electron transfer system of photo(electro)catalytic N_2 reduction on the $Fe_2Ti_2O_7$ thin film includes a series of processes of nitrogen-diazene-hydrazine-ammonia-nitrate. Moreover, Lashgari proposed a N_2 photofixation mechanism based on H-atom production [40]. In addition to Fe doped metal oxide materials, non-metal oxide semiconductors were modified with iron. Hu et al. adapted graphitic carbon nitride doping with Fe^{3+} for conversion of nitrogen to ammonia [41]. It was found that the N≡N bond is prolonged when N_2 molecules interact with Fe^{3+} sites. The delocalization of electron in σ_g2p orbital (HOMO) of nitrogen when N_2 adsorbed on Fe^{3+} doping sites leads to its orbital energy almost overlaps to that of πg*2p orbital (LUMO), indicating the direct role of iron in activating the N_2 molecule. The highest NH_4^+ production rate of 5.4 $mgL^{-1}h^{-1}g^{-1}$ was achieved with 0.05 wt% Fe doping, which is 13.5 folds compared to pristine g-C_3N_4. For the comparison of photocatalytic activities of ammonia production based on iron active site photocatalyst, the selected literature report is summarized in Table 2.

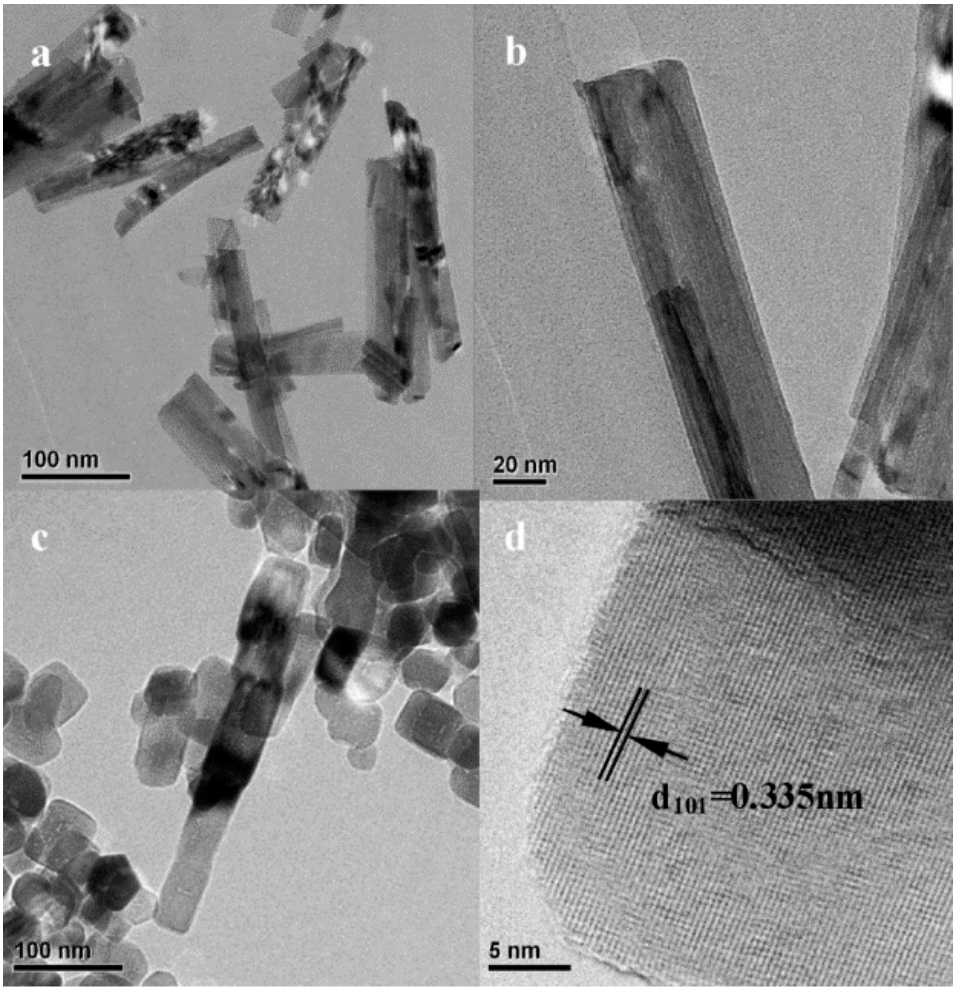

Figure 5. (**a**,**b**) TEM images of titanate nanotubes prepared by hydrothermal reaction. © transmission electron microscopy (TEM) images and (**d**) high resolution transmission electron microscopy (HRTEM) image of 100 × 10^{-6} Fe^{3+} doped TiO_2. (Reproduced with permission from Elsevier [36]).

Table 2. Summary of iron active site photocatalysts for the reduction of N_2 to NH_3.

Catalyst	Light Source	Sacrificial Reagent	NH_3 Rate	Ref.
0.2% Fe-doped TiO_2	390–420 nm	-	10 $\mu mol g^{-1} h^{-1}$	[42]
0.5% Fe-doped TiO_2	UV	-	6 $\mu mol g^{-1} h^{-1}$	[37]
Fe-doped TiO_2	254 nm	Ethanol	400 $\mu M \cdot h^{-1}$	[36]
Partially reduce Fe_2O_3	UV-vis	-	10 $\mu mol g^{-1} h^{-1}$	[34]
Fe_2O_3	UV-vis	Ethanol	1362.5 $\mu M \cdot h^{-1}$	[40]
$Fe_2O_3 \cdot nH_2O$	Visible	-	6 $\mu M \cdot h^{-1}$	[34]
Fe(O)OH	Vis	-	9.25 $\mu M \cdot h^{-1}$	[43]
Fe doped C_3N_4	Vis	Ethanol	120 $\mu M \cdot h^{-1}$	[41]
Fe-load 3D Graphene	UV	-	24 $\mu mol g^{-1} h^{-1}$	[44]
Hydrous oxide of Fe and Ti	Vis	-	22 $\mu M \cdot h^{-1}$	[45]
Iron loaded bentonite	UV	-	1.33 $\mu M \cdot h^{-1}$	[46]
Iron titanate thin film	>320 nm	Ethanol	0.57 $\mu M \cdot h^{-1} cm^{-2}$	[38]

4.1.2. Titanium Active Sites

Among all the well-known photocatalysts, TiO_2 is the most prominent material and has applied in a variety of photocatalytic applications, because of its abundance, efficient charge separation, and stability. In earlier publications, the metal doped titanium dioxide or titanate was used for photocatalytic fixing nitrogen. In later studies, trivalent titanium complex has been employed to promote the N≡N cleavage [47,48]. Figure 6a illustrates a typical role of Ti^{3+} reacted with N_2 via electron donation. These reduction reactions create Ti^{4+}-amine complexes which finally release NH_3 with regenerated trivalent Ti^{3+} complexed. Inspired by this suggestion, Hirakawa et al. have successfully synthesized reduced titania with Ti^{3+} defects, which served as the adsorption sites for N_2 and trapping sites for the photogenerated electron [49]. The proposed mechanism is shown in Figure 6b. The solar-to-conversion efficiency is 0.02%. However, it is still lower than that of natural- and artificial-photosynthesis, therefore, an improvement of that material in photocatalytic activity is necessary.

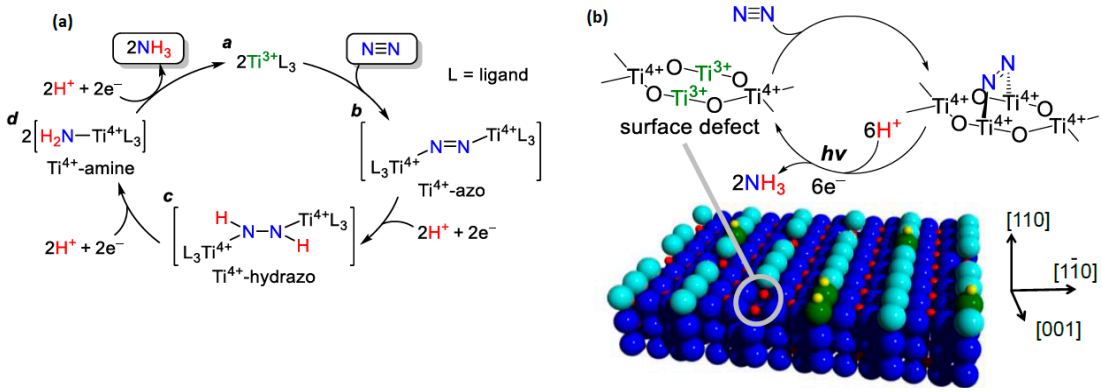

Figure 6. Scheme (**a**) catalytic cycle for N_2 fixation by Ti^{3+}-containing; Scheme (**b**) proposed photocatalytic cycle for N_2 fixation on the rutile. (Reproduced with permission from ACS [49]).

4.1.3. Molybdenum Active Sites

Owing to excellent electrical, optical, and photovoltaic properties, ultrathin transition metal dichalcogenides (TMDs) have been considered as promising materials. Among them, MoS_2 semiconductor is known as an efficient photocatalyst for hydrogen evolution and CO_2 conversion reaction. Recently, its application in N_2 reduction has been unveiled since the first report of Sun's group [50]. In this research, the photocatalytic activity of MoS_2 photocatalysts under different preparation conditions was investigated. The results show that the sonicated ultrathin MoS_2 induced charged excitons (trions) when applying visible light (Figure 7a). These trions carried multiple

electrons in one bound state, which located around Mo sites. Naturally, three Mo atoms surround adsorbed dinitrogen on the S vacancy and facilitate the six-electron transfer process. Consequently, the rate of ammonia production of 325 μmol.g^{-1}h^{-1} was achieved, which is much higher than the rate of hydrothermal MoS_2 and bulk MoS_2 samples. Particularly, it can be concluded that a multiple electrons reduction process was responsible for the enhancement of photocatalytic dinitrogen reduction to ammonia.

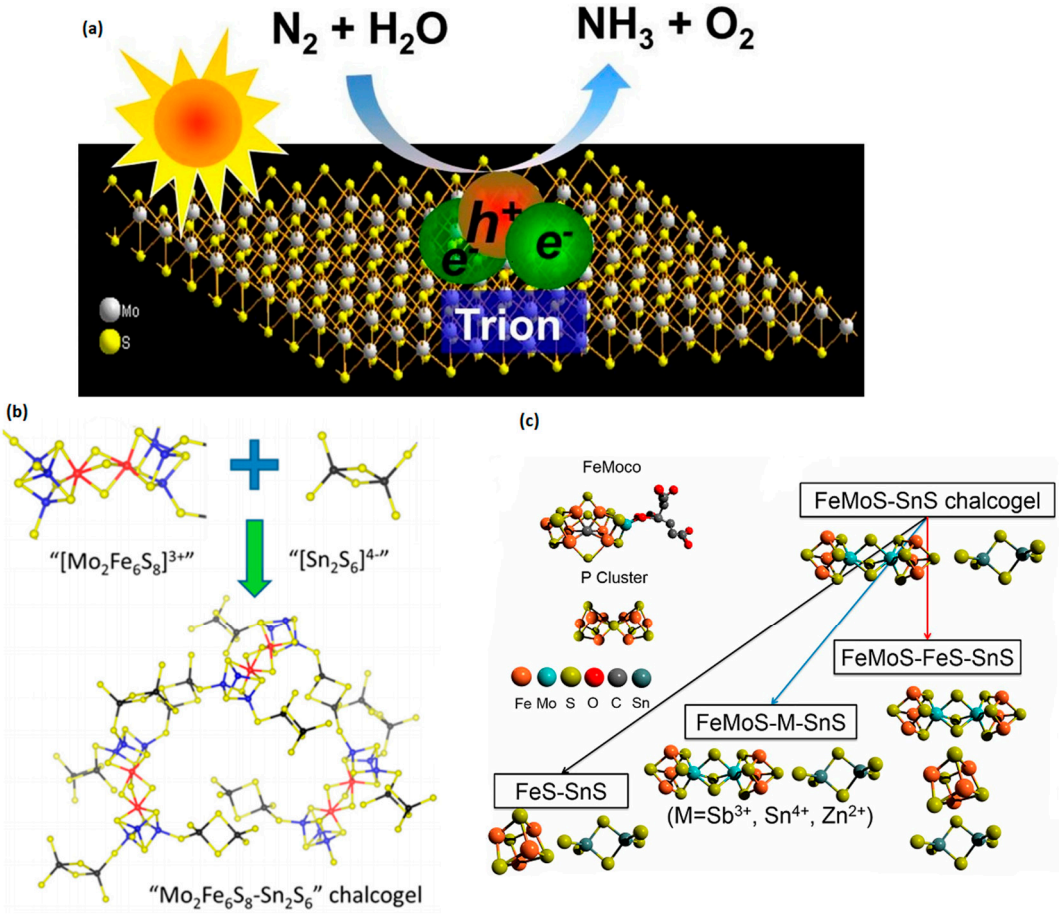

Figure 7. (**a**) Schematic illustration of the trion induced multi-electron N_2 reduction process [50]; (**b**) Schematic representation of $Mo_2Fe_6S_8$—Sn_2S_6 biomimetic chalcogel (FeMoS chalcogel), building block scheme (Mo, blue; Fe, red; S, yellow; Sn, black), and a complete chalcogel shown at right [51]; and (**c**) Nitrogenase-inspired biomimetic chalcogels [52]. (All the figures are reproduced with permission from the respective publishers).

In addition, enzyme nitrogenase has also been widely studied for application of catalytic nitrogen fixation [53]. A nitrogenase is a two-component system comprising a MoFe protein and an associated Fe protein. Based on this inspiration, in 2015, Banergee and Kanatzidis supposed that solid chalcogels consisiting of FeMoS inorganic clusters is able to reduce dinitrogen to amonia by utilizing white light [51]. The double-cubane $Fe_2Mo_6S_8$ units were associated by Sn_2S_6 ligands (Figure 7b) to form a stable amorphous complex in aqueous solution. The FeMoS cluster (FeMoS cofactor, a synthetic clusters bearing Mo−Fe linkages) of the biomimetic chalcogel system is a structural and functional analogue of the MoFe active site in the enzyme nitrogenase. This work showed that the high density of FeMoS active sites can boost multi-electron transformation as well as mimic the function of biological nitrigenases in N_2 fixation. In order to gain insights into the performance of the FeMo cofactor in nitrogenases. Brown and coworkers fabricated a biohybrid system of nitrogenase coupled with CdS semiconductor. The MoFe protein coated CdS nano rods produced 315 nmol of NH_3 per min over one

mg MoFe-protetin, which is estimated for 3.3% of Quantum Yield. In MoFe Protein, FeMo cofactor plays a role as an active site, receiving photogenetated electrons from CdS nanocrystals. By changing condition reactions, Liu found that lack of FeMo cofactor did not produce amonia. Furthermore, the role of Mo and Fe in the MoFe protein are revealed in another study. Liu et al. discussed the photocatalytic activity of nitrogen reduction by the nitrogenase-inspired biometic chalcogel [52]. In this system, $Mo_2Fe_6S_8(SPh)_3$, Fe_4S_4 and redox-inert ions are assembled with Sn_2S_6 (Figure 7c). However, iron was expected to be more active than molybdenum for the solar reduction of N_2, due to the fact that a weak bonding orbital between nitrogen and iron emerged via the localized orbital analysis. Moreover, their conclusion that the Fe is a better active site for N_2 binding than Mo has been demonstrated by recent biochemical and spectroscopic data.

4.1.4. Nickel Active Sites

The study of Schrauzer and Guth examined the effect of various metal dopant over titania for photocatalytic NH_3 formation. In addition to doping Mo and Fe, only Co and Ni dopant performed the contribution to the enhancement of NH_3 production efficiency [42]. The other metal doped, such as Pd, V, Cu, showed no improvement in catalytic activity. It can be explained by the influence of Ni, Co accelerates the phase transformation while this phenomenon is unobtainable for other dopants. This explaination is consistent with the conclution of Ranjit. In his work, Ranjit also compared 12 elements doped TiO_2 photocatalyst and found the order of photoactivity was Fe > Co > Mo > Ni. Ye et al. loaded Ni_2P on a binary metal sulfide solid solution for photocatalytic N_2 fixation under visible light [54]. The deposited transition metal phosphide affects both the VB and CB of metal sulfide, resulting in higher photocatalytic reduction ability. Moreover, the transition metal phosphide of Ni_2P supports the photo-induced charge carrier separation process, which is confirmed by photoluminescence spectra (PL) and electrochemical impedance spectroscopy (EIS)For $Ni_2P/Cd_{0.5}Zn_{0.5}S$, the NH_3 production rate achieved 101.5 μmol L^{-1} h^{-1} (35.7 times than that of unloaded metal phosphine cocatalyst), corresponding to 4.23% of apparent quantum efficiency at 420 nm.

4.2. Non-Metal Vacancies

4.2.1. Oxygen Vacancies

In the earlier studies, the synthesis of ammonia by N_2 photoreduction has been far from acceptable, because of the impoverished binding of N_2 to catalytic active sites and the high energy of the intermediates required in the reactions. It has been concerned a significant challenge of activation and cleavage of the highly stable N≡N triple bond relying only on light-induced electrons from semiconductor materials in solar-driven N_2 fixation. To conquer this challenge, the electron-transfer supportive centers should be introduced as the primary-step active sites to absorb the molecular N_2 and weaken the N≡N bond, which could allow the photo-induced electrons to inject for the subsequent reduction reactions. Oxygen vacancies (OVs), with their rich localized-electrons, have been proved to serve as electron trapping centers that can effectively capture and activate the inert gases, such as O_2, CO_2, and N_2 in particular. Table 3 summarizes the most recent advanced oxide materials containing Ovs for nitrogen photo-fixation.

Table 3. Summary of oxide catalysts for the photoreduction of N_2 to NH_3.

Catalyst	Light Source	Sacrificial Reagent	NH_3 Rate	Ref.
BiOBr nanosheets	UV-Vis/Vis	-	104.2 μmol$g^{-1}h^{-1}$	[31]
Bi_5O_7Br nanotubes	Vis	-	1.38 mmol·g^1h^{-1}	[55]
TiO_2/Au/a-TiO_2	Vis	-	13.4 nmol $cm^{-2}h^{-1}$	[56]
BiO quantum dots	UV-Vis	-	1226 μmol$g^{-1}h^{-1}$	[57]
Reduced TiO_2	Infrared light	-	3.33 μmol$g^{-1}h^{-1}$	[58]

Table 3. *Cont.*

Catalyst	Light Source	Sacrificial Reagent	NH_3 Rate	Ref.
Rutile TiO_2	λ > 280 nm	2-Propanol	16.67μM·g^1h^{-1}	[49]
BiOCl nanosheets	Solar Light	Ethanol	45 μM·h^{-1}	[59]
Bi_5O_7I nanosheets	280–800 nm	Ethanol	120 μM·h^{-1}	[60]
CuCr–LDH	Vis	-	57.1 μmol$g^{-1}h^{-1}$	[61]
Hydrogenated Bi_2MoO_6	Solar light	-	1.3 mmol·$g^{-1}h^{-1}$	[62]

Oxygen Vacancies Based on Titanium Dioxide

Recently, Zhang et al. created solid-state sources of solvated electron based on reduced titanium dioxide for nitrogen photofixation [55] (Figure 8). Since oxygen vacancies were introduced in TiO_2, electrons are trapped at the vacancy sites and released by infrared (IR)-light excitation, consequently reducing N_2 to NH_3. The number of trapped electrons can be enriched by tuning the concentration of oxygen defects. However, the amount of generated ammonia nearly ceased after 24 h, due to the consumption of releasable trapped electron. For recharging of electrons, the reacted TiO_2 could be treated with chemical reduction method.

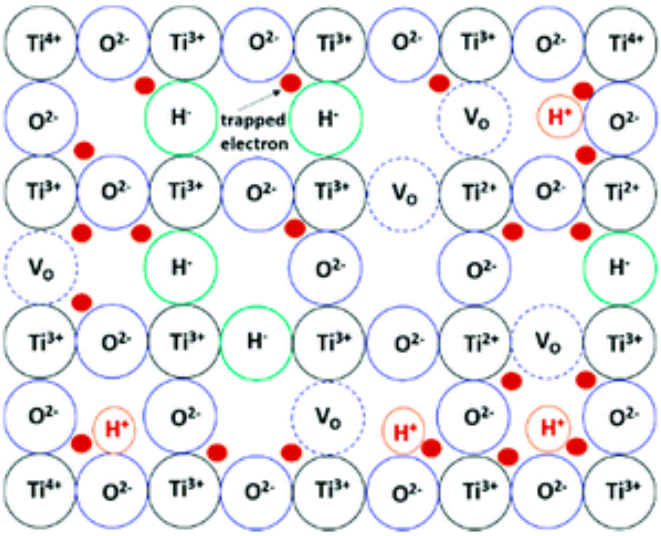

Figure 8. Schematic illustration of the main defects existing in reduced TiO_2 upon boron hydride reduction. (V_O: Oxygen vacancy; H^-: Hydride anion in lattice oxygen site; H^+: Proton bonding with lattice oxygen.) The trapped electrons are also illustrated. (Reproduced with permission from RSC [58]).

Another group, Li, and his partner conducted the photo-electrochemical reduction of N_2 to NH_3 on the surface oxygen vacancies of plasmon-induced TiO_2 [56] (Figure 9). Li suggested that only superficial oxygen vacancies can act as active sites, the other internal vacancies in crystal structure play a role as undesired defects. By using the atomic layer deposition method, oxygen vacancies are successfully introduced onto the surface of TiO_2 without creating bulk defects (introduction of oxygen vacancies to bulk structure to form defects). It is worthy to note that surface oxygen vacancies not only serve as N_2 absorption sites, but also promote charge-carrier transportation to the adsorbed nitrogen while bulk-vacancies act as recombination centers to trap the photo-excited electrons and holes. The optimized ammonia production rate of 13.4 nmol $cm^{-2}h^{-1}$ was obtained by the sample of surface oxygen vacancies modified TiO_2/Au/amorphous TiO_2 electrode, which is 2.6-folds higher than pristine TiO_2. Moreover, Hirai and his group have studied systematically the role of oxygen vacancy and Ti^{3+} active site [49]. He concluded that oxygen vacancy can facilitate the dissociation of the N≡N triple bond. This conclusion is consistent with Zhang and Li's group.

In contrast with the above research, Medford and Comer employed density functional theory (DFT) analysis to discuss the role of oxygen vacancy [63]. The defected surface (110) titania possessing an oxygen vacancy was compared to pristine TiO_2 by examining nitrogen reduction. The DFT calculations rejected the traditional mechanism of nitrogen photofixation that the breaking of N-N bond is conducted directly by oxygen vacancy. Otherwise, his hypothesis is that a considerable stabilization of the unstable NH_x intermediates by the oxygen vacancy makes NH_x binding close to exo-thermic, indicating that it can enhance nitrogen reduction and ammonia generation after the N–N bond has been dissociated.

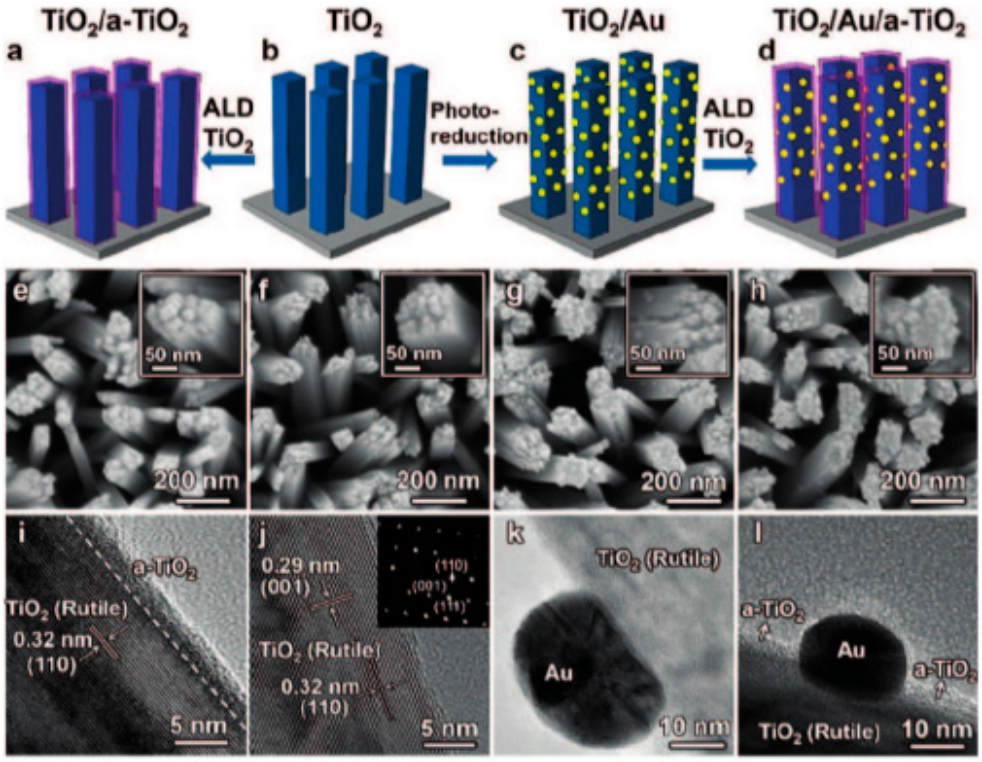

Figure 9. (**a**–**d**) Illustration of the experimental procedures for preparation of bare TiO_2, TiO_2/Au, TiO_2/a-TiO_2, and TiO_2/Au/a-TiO_2 photo-electrodes. (**e**–**h**) Scanning electron microscopy (SEM) and (**i**–**l**) HRTEM images of photoelectrodes. Key: TiO_2/a-TiO_2 (**a**,**e**,**i**), bare TiO_2 (**b**,**f**,**j**) (inset:selected area electron diffraction (SAED) pattern of the bare TiO_2 NR), TiO_2/Au (**c**,**g**,**k**), TiO_2/Au/a-TiO_2 (**d**,**h**,**l**). (Reproduced with permission from Wiley [56]).

Oxygen Vacancies Based on Bismuth Oxyhalide

Bismuth oxyhalides, BiOX (X = Cl, Br, and I), have recently gained considerable interests for their intrinsic optical properties; they are also practical for industrial applications, such as the photodecomposition of organic pollutants and CO_2 reduction. The structural layer of BiOX provides sufficient space for the polarization of atoms and the as-formed internal electric field will play an effective role in their efficient charge separation and transfer process.

Due to containing interior oxygen vacancy, bismuth oxyhalides has been considered as a promising catalyst for nitrogen fixation, particularly in photofixation [64,65]. Most recently, Bi_5O_7Br nanotubes were investigated its photoactivity of ammonia evolution by Wang et al. [55]. Owing to the excessive number of oxygen vacancies as active centers, the highest NH_3 production rate is obtained at 1.38 mmol·$g^{-1}h^{-1}$, corresponding to an apparent quantum yield of 2.3% at 420 nm. However, bismuth oxybromide photocatalysts are susceptible to photocorrosion. During the reduction reaction, the oxygen vacancies is filled by O atoms form the water, reducing the number of active sites and lose its activity. Interestingly, the reacted oxygen vacancies can be regenerated by applying visible light

illumination, which continuously provides the reversible light-switchable surface oxygen vacancies for N_2 fixation. Figure 10A demonstrates repeated circulation of oxygen vacancies over TiO_2 for ammonia photo-production.

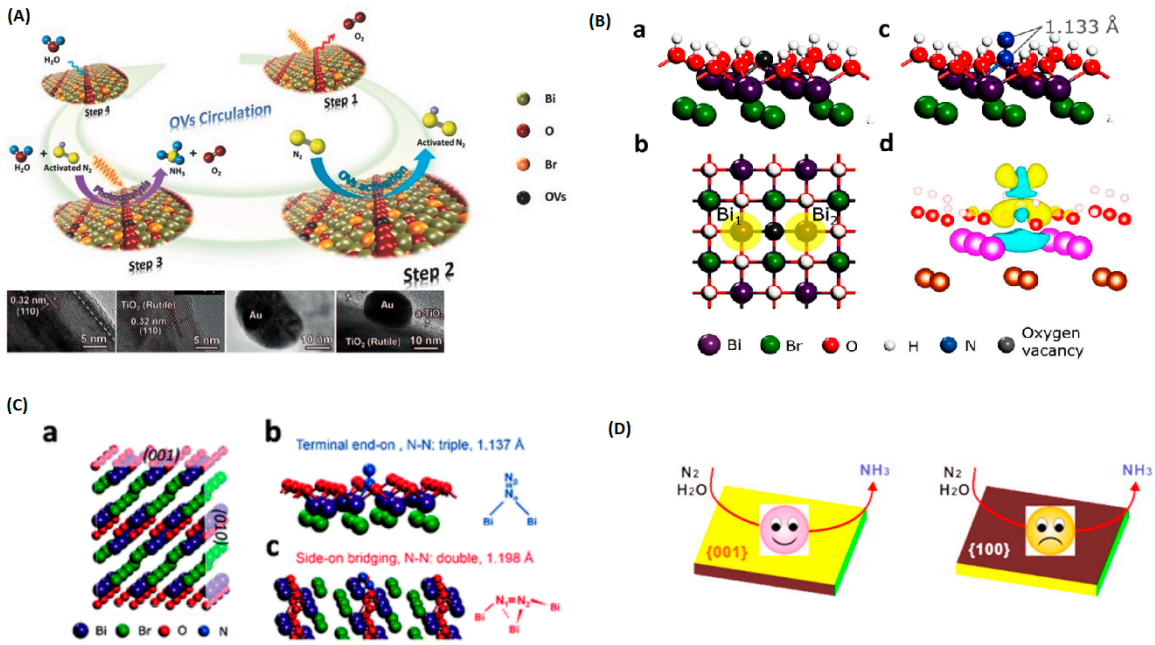

Figure 10. (**A**) Schematic illustration of the photocatalytic N_2 fixation model in which water serves as both the solvent and proton source, as well as the reversible creation of light-induced oxygen vacancies; (**B**) Theoretical prediction of N_2 activation on the OV of BiOBr (001) surface. (a) Side and (b) top view of (001) surface of BiOBr with an OV. (c) The adsorption geometry of N_2 on the OV of BiOBr (001) surface. (d) The charge density difference of the N_2-adsorbed (001) surface; (**C**) Adsorption of N_2 on the (001) and (010) facets of BiOCl. (a) Crystal structure of BiOCl and the corresponding cleaved (001) and (010) surface. (b) The terminal end-on adsorption structure of N_2 on (001) surface of BiOCl and (c) the side-on bridging adsorption structure of N_2 on (010) surface of BiOCl; (**D**) Schematic illustration of the photocatalytic N_2 fixation over Bi_5O_7I (001) and (100) facers. (Reproduced with permission from the respective publishers; Figures 10–10 from the References [55], [31], [59], and [60], respectively).

In 2015, Zhang and Li studied the effect of oxygen vacancies on the exposed (001) facets BiOBr nanosheets to fix nitrogen under ambient condition [31]. The theoretical analysis calculated the extension of the N–N triple bond increased by 0.055 Å as absorbed N_2 molecules are activated by oxygen vacancies (Figure 10B). Also, the oxygen vacancies as the initial electron acceptor can avoid the electron-hole recombination and considerably promote the interfacial charge transfer. In this paper, the UV-Visible light driven N_2 fixation rate was measured to be 223.3 $\mu mol g^{-1} h^{-1}$ without using sacrificial agent and a noble-metal cocatalyst. As a succession of the previous study, Zhang's group clarified that two distinct structure of surface oxygen vacancy on different facets of BiOCl nanosheets completely determine the N_2 fixation mechanisms [59]. For instance, the N_2 reduction reaction on the oxygen vacancies of BiOCl (010) facets followed a symmetric alternating pathway which generates N_2H_2-level and N_2H_4-level species. Whereas, an asymmetric distal mechanism selectively produces ammonia (001) facets without involving the generation of N_2H_2 or N_2H_4. By DFT calculation, the accepted adsorption possibility of N_2 on BiOCl surfaces was investigated. On the (001) facets, absorbed N_2 combines with two nearest Bi atoms in the sublayer to form a terminal end-on bridging, consequently, the activation exhibited the increasing N–N bond length to 1.137 Å (Figure 10(Ca)). Separately, different absorbed N_2 performs a larger extent of N_2 activation and elongates bond length to 1.198 Å (Figure 10(Cb)) through a side on bridging mode (dinitrogen interacts with two nearest Bi atoms in the outer layer and the one next nearest Bi atom in the sub-layer on the (010) facet).

Respectively, the quantum yields under UV irradiation were 1.8% h^{-1} and 4.3% h^{-1} on the (001) and (010) surface of BiOCl. Inspired by Zhang's group, Bai et al. examined the photocatalytic activity of different Bi_5O_7I facets over solar-driven N_2 fixation reaction [60]. At 356 nm UV-light irradiation, the apparent quantum efficiency of (001) surface Bi_5O_7I was 5.1%, which is 2.2 times higher than that of (100) planes (Figure 10D). After exposure to (001) facets, the charge carrier separation and mobility were dramatically boosted, elucidating the enhancement of photoactivity on (001) Bi_5O_7I facets.

Although most publications highlight noteworthy attention on the exposure of different facets, it is more possible that the combined effects facet-dependent studies and oxygen vacancies-dependent studies will open a new and interesting perspective and provide inspiration for the development of advanced photocatalysts for N_2 photoreduction. In addition, the combination of experimental data and theoretical simulations is highly necessary to fully interpret the N–N triple bond activation and pathway the NH_3 formation mechanism. Thus, further study on the facet controlled and vacancy-mediated bismuth oxyhalides should be dedicated in the future to emphasize the scientific aspects and reveal the appropriate reaction steps for the N_2 photofixation.

4.2.2. Nitrogen Vacancies

The introduction of defects in photocatalyst materials is completely considered as an effective method to enhance the photocatalytic nitrogen fixation. Instead of oxygen vacancy, another alternative strategy for using non-metal vacancy to fix nitrogen has been to utilize nitrogen vacancies in order to absorb and weaken N_2 molecules. Because nitrogen vacancies have the same size and shape as the nitrogen atoms in di-nitrogen, nitrogen vacancies (NVs) are favorable in the selective chemisorption and activation of N_2 [66]. This interprets why the N_2 fixation rate remained unchanged when N_2 was replaced by air as the N_2 source. In addition, nitrogen vacancies significantly improved the separation of charge carriers by trapping photo-excited electrons and facilitating the interfacial charge transfer to the adsorbed N_2.

From the time when the first report on graphitic carbon nitride (g-C_3N_4) in 2009, this metal-free polymeric photocatalyst has received tremendous interest, due to its specific properties such as excellent stability, cost-effectiveness, and environmental benignity. Recently, graphitic carbon nitride composing of nitrogen vacancies has been employed as a photocatalyst for reduction of nitrogen to ammonia. In 2015, the first introduction of nitrogen vacancies induced g-C_3N_4 for visible light driven NH_3 production was reported by Dong [66]. After 15 h of light illumination, nitrogen vacancies incorporated g-C_3N_4 generated 1.24 $mmolh^{-1}g^{-1}$ of photofixation rate while bare g-C_3N_4 show no catalytic activity, suggesting the indispensable role of nitrogen vacancies in promoting photoactivity. However, lacking nitrogen in defects modified carbon nitride structure slightly enlarged bandgap energy than that of pristine samples, resulting in a reduction of visible light absorption ability. In contrast to Dong's research, Li suggests that even the influence of nitrogen vacancies on the band structure decrease the bandgap energy, it is not the main factor that affects the photocatalytic nitrogen reduction. Li et al. have fabricated nitrogen vacancies assisted g-C_3N_4 by infrared ray assisted microwave (IM-CN(x), where x denots the time) [67]. Under microwave treatment, abundant nitrogen vacancies were formed and served as chemical absorption centers. By DFT calculation, it was found that chemisorbed N–N triple bond is elongated from 1.107 Å to 1.242 Å due to the formation of σ bond between N_2 molecule and the nearest C atom. Consequently, the NH_4^+ evolution rate obtained by IM-CN(30) sample was 5.1 mg L^{-1} h^{-1} $gcat^{-1}$, which is 5-fold and 2.5-fold higher than those of bulk CN_{520} and microwave treated CN(20). Similarly, Ma and Li have prepared high specific surface area carbon nitride by a dissolve-regrowth method, which is capable of N_2 photoreduction [68]. Based on experimental results and theoretical simulation, Ma demonstrated the possible nitrogen photofixation over large surface area g-C_3N_4 containing N-vacancies (Figure 11). First, absorbed N_2 molecule in N-vacancy is activated by four-electron which occupies the anti-bonding orbitals of N atoms, then H^+ reacts with the activated N_2 molecule to produce NH_3 and finally form NH_4^+.

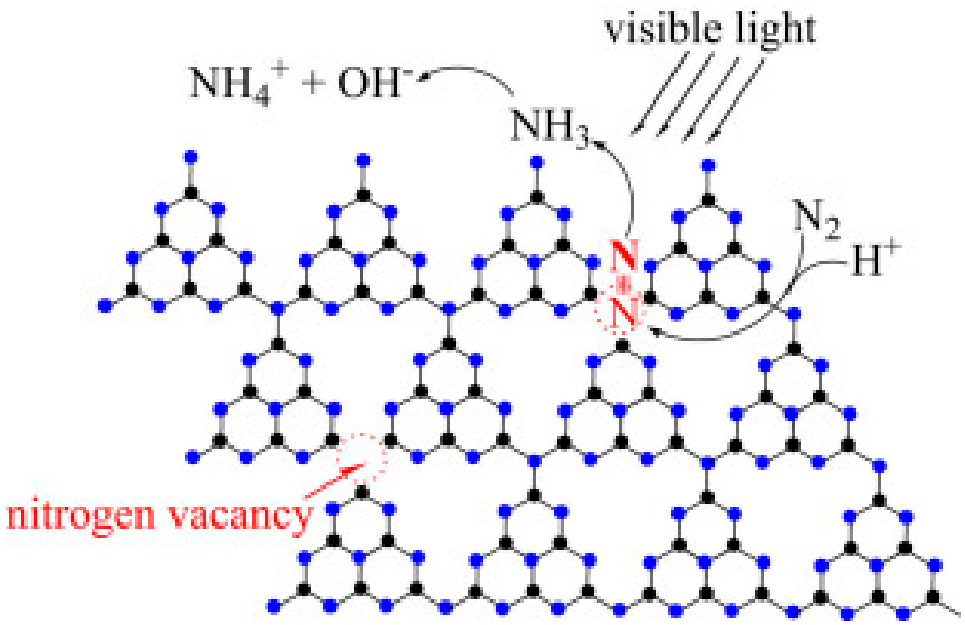

Figure 11. The possible nitrogen photofixation process proposed by Ma et al. (Reproduced with permission from Elsevier [68]).

Besides using nitrogen vacancy active sites, nitrogen defects is also applied for producing NH_3 under solar simulation. Li et al. introduced cyano-deficient onto bulk g-C_3N_4 by cleavage C=N bond via KOH etching treatment [69]. The as-prepared g-C_3N_4 (ACN) possesses a porous structure with ladder-like thin layers. Li concluded that the presence of cyano groups not only reduce conduction band of bulk g-C_3N_4, but also act as an electron acceptor, capturing electrons and inhibiting electron-hole recombination. Moreover, the existent of cyano defects conduct more adsorption site for the N_2 activation. Therefore, the formation of cyano groups by etching bulk g-C_3N_4 with KOH is the main reason for the enhanced photocatalytic N_2 fixation activity. After 4 h testing catalytic activity, the NH_4^+ concentration of ACN-10% increase to 51.65 mg/L, which is 7.6 times higher than bulk samples. Figure 12 shows the formation of cyano deficient g-C_3N_4 and N_2 photofixation mechanism.

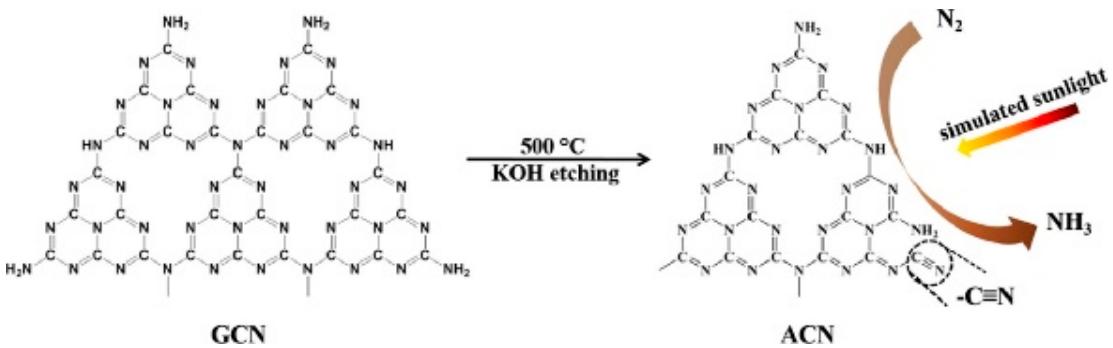

Figure 12. The cyano defects were successfully introduced into the g-C_3N_4 framework by KOH etching and could contribute to improving the nitrogen photofixation ability of g-C_3N_4. (Reproduced with permission from Elsevier [69]).

4.2.3. Sulfur Vacancies

Due to similar chemical properties with oxygen, Hu hypothesized that sulfur vacancies have N_2 absorption ability as oxygen vacancies [70]. In his study, a tri-component metal sulfide of $Zn_{0.1}Sn_{0.1}Cd_{0.8}S$ was prepared by the hydrothermal process. Under visible light irradiation, the photocatalyst performs an outstanding activity in nitrogen fixation, because of containing a

high concentration of sulfur vacancies. This research implied that the photocatalytic nitrogen fixation activity is linearly depended on the sulfur vacancy concentration. The NH_4^+ production rates over the various vacancy concentrations were compared and illustrated in Figure 13a, confirming that the concentration of sulfur vacancies plays a significantly pivotal role in the N_2 photofixation ability.

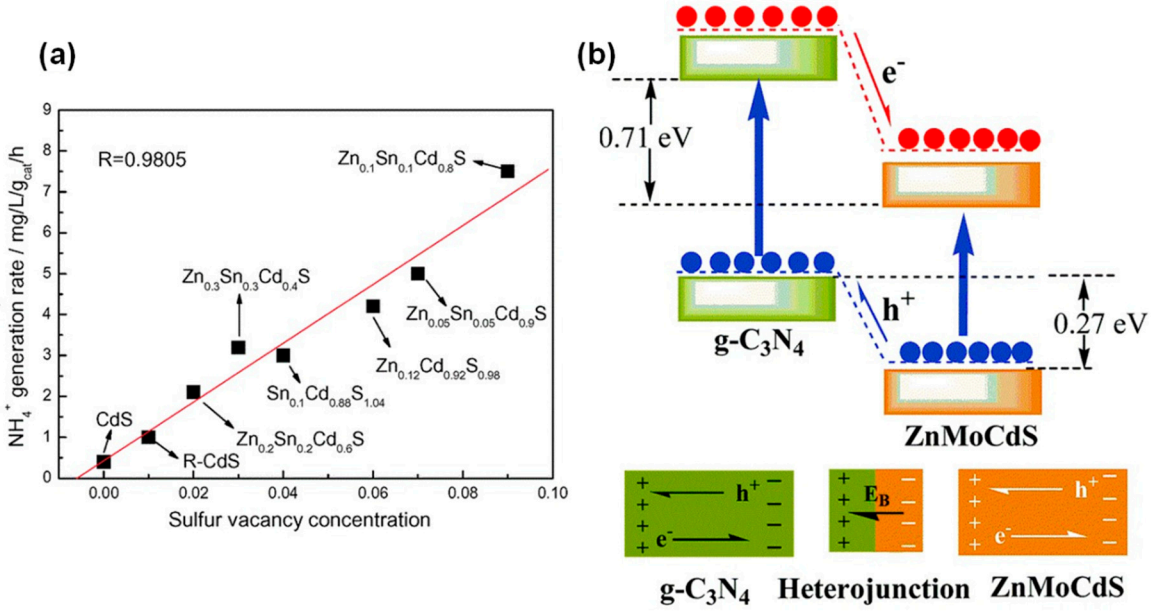

Figure 13. (**a**) Nitrogen photofixation performance of the as-prepared catalysts as a function of the sulfur vacancies concentration [70]; (**b**) The schematic of electron–hole separation and transport at the g-C_3N_4/ZnMoCdS heterojunction interface [71]. (Reproduced with permission from the respective publishers).

Hu also discussed the role of Zn, Sn metal doping in the creation of sulfur vacancies rather than act as active sites to promote catalytic ability. The proof of elongated N–N triple bond from 1.164 Å to 1.213 Å over sulfur vacancies proves that sulfur vacancies can aid the activation of N_2 instead of doped metal. In this regard, Hu's group continues to investigate the effect of different metal doping on ternary metal sulfide. Mo and Ni doped CdS can distort the crystal structure, leading to the formation of sulfur vacancies in obtained tri-component metal sulfide [72]. In order to compare the influence of sulfur vacancies, the as-prepared samples were calcined in O_2 gas to remove sulfur vacancies. In results, the photocatalytic NH_4^+ generation rates of $Mo_{0.1}Ni_{0.1}Cd_{0.8}S$ photocatalyst is 3.2 mg L^{-1} h^{-1} $gcat^{-1}$, which is 10-folds higher in comparison with the oxidized sulfur vacancies sample of $Mo_{0.1}Ni_{0.1}Cd_{0.8}SO$. Hu concluded that the sulfur vacancies not only act as chemical absorption sites, but also capture photo-generated electrons, suppress charge recombination and encourage interfacial charge transfer.

A strategy of coupling carbon nitride with sulfur vacancies doped metal sulfide was applied for the reduction of N_2 under visible light. At the same time, two similar heterojunction system of g-C_3N_4/ZnSnCdS and g-C_3N_4/ZnMoCdS were assembled by Cao et al. [71,73]. In general, the photo-induced electrons will be excited and migrated from g-C_3N_4 to the quaternary metal sulfide whereas the photo-generated holes are transferred in the reversed direction and consumed by hole scavenger. Additionally, the sulfur vacancies could trap immigrated electrons form g-C_3N_4 and intrinsic electrons in metal sulfide then transport immediately to activated N_2. The schematic of electron-hole separation and transportation is depicted in Figure 13b. As the photoinduced electrons and holes are spatially separated, the charge recombination will be drastically inhibited, which is of highly beneficial for enhancing the photocatalytic activity. Under visible light irradiation, the highest NH_4^+ evolution rates of g-C_3N_4/ZnSnCdS and g-C_3N_4/ZnMoCdS are 7.5 and 3.5 mg L^{-1} h^{-1} $gcat^{-1}$, respectively, which is 33.3 and 13.5 times higher compared to those of individual g-C_3N_4.

4.3. Metal Cocatalyst and Plasmon Enhancement

4.3.1. Metal Cocatalyst

In addition to the introduction of interior active sites, transition metals can be employed as exterior active sites by loaded on the semiconductor photocatalysts, namely cocatalyst. Cocatalysts play a critical role in photocatalysis. As electron acceptor, cocatalysts promote electron-hole separation and impede photogenerated charge carrier recombination. Among a variety of cocatalyst, platinum and ruthenium have been considered as the most effective cocatalyst, particularly in hydrogen evolution and CO_2 conversion. Inspired by prior research, Miyama engaged Pt loading TiO_2 and CdS for the improvement of N_2 photoreduction [74]. For both TiO_2 and CdS, the yield of ammonia was increased approximately 1.5 times after introducing noble metal cocatalyst. Several years later, Mirza group applied both Pt and RuO_2 as a reduction and oxidation cocatalyst in CdS [75]. The Pt particles in this system act as electron trapping centers which capture photoexcited electrons and perform reduction reaction. Whereas, the RuO_2 serves as a hole scavenger to consume generated hole, balancing electric charge. Figure 14a demonstrates the mechanism of photocatalytic ammonia evolution based on CdS/Pt/RuO_2 photocatalyst.

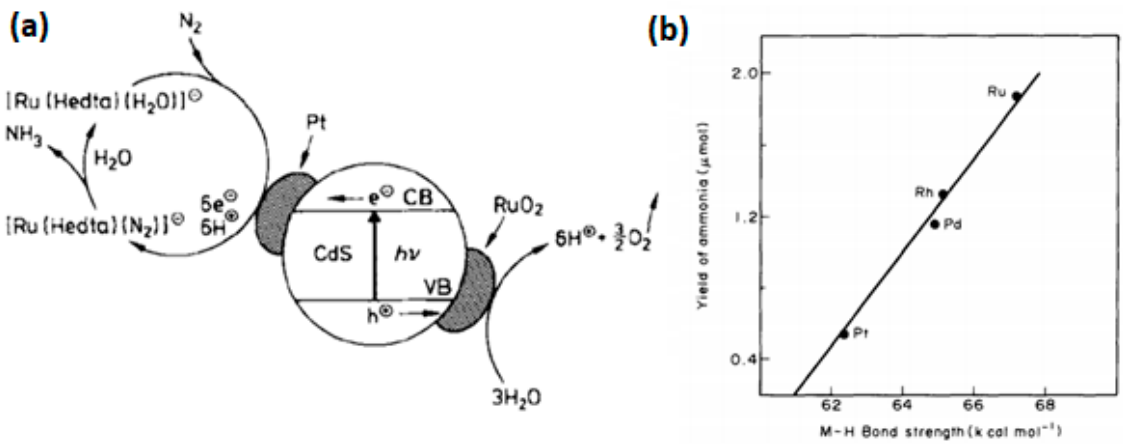

Figure 14. (**a**) the mechanism of photocatalytic N_2 fixation over CdS/Pt/RuO_2 [75]; (**b**) M–H bond Strength vs. yield ammonia [76]. (Reproduced with permission from the respective publishers).

In 1996, Ranjit et al. systematically investigated the impact on photocatalytic NH_3 evolution by the nature and amount of four noble metals decorated TiO_2 [76]. It is worth noting that ammonia was not produced by using pure TiO_2 photocatalyst. However, the metallization of titania results in the increasing of ammonia generation rate. It was found that the production rate is depended on several factors. First, the noble metals form the ohmic contact with semiconductor and serve as electron sinks where can easily accommodate the flow of electron transfer, suppressing electron-hole recombination. Secondly, the report supposed that the key role of the installed metal is to stabilize H_{ads} formed on the metal, thus enhancing the ammonia yield. Figure 14b illustrates the linear dependent between the Metal-H_{ads} bond strength and the yield of ammonia. This proposal is consistent with another work investigating Ru, Fe, and Os cocatalysts [77], where it was found that metal cocatalysts for NH_3 production needed to have a high over-potential for H_2 evolution; where the metals with high over-potentials for the hydrogen evolution reaction (Ru and Fe) having higher NH_3 activity than the metals with low hydrogen evolution reaction over-potential. Based on experimental data, Ranjit deduced that the catalytic activity of the nanocomposite photocatalyst is observed in the trend Ru > Rh > Pd > Pt. It is clearly seen that the trend is reversed in the hydrogen evolution reaction. Medford suggested that the role of the metal site is to minimize hydrogen evolution rather than being a cocatalyst for NH_3 synthesis [78].

4.3.2. Plasmon Enhancement

A fundamentally different approach for loading transition metal supported fixing nitrogen has been demonstrated to enhance light absorption through the surface plasmonic enhancement [79–83]. In order to increase the NH_3 production rate by harnessing the localized surface plasmon resonance, most recent studies have focused on using gold nanoparticles as a plasmonic structure. Owing to high light-harvesting properties, gold in a nanoparticle can absorb visible light and induce surface plasmon effect, which can inject hot electrons into the semiconductor conduction band. Oshikiri and his partner assembled a photoelectrode, with Au nanoparticles and Ru cocatalyst co-loaded Nb-$SrTiO_3$ [80]. The hypothesized mechanism was proposed that the excited hot electron is transferred to $SrTiO_3$ semiconductor and continuously injected into Ru cocatalyst. At the Ru surface, nitrogen and proton are reduced to ammonia. In contrast, the generated holes localize near the Au/Nb-$SrTiO_3$/water interface and immediately oxidize hydroxyl ions and ethanol (Figure 15a). The ammonia production was observed at long wavelengths up to 800 nm, implying plasmon-induced charge separation promoted nitrogen reduction in the cathode and oxidation in the anodic side. However, Ru cocatalyst not only accelerates N_2 reduction, but also for H_2 evolution because of stable absorption of H_2 onto a Ru surface. Later, a replacement of Ru cocatalyst with Zr/ZrO_x cocatalyst was reported by the initial group in 2016 [81]. In the Au/Nb-$SrTiO_3$/Zr/ZrO_x system, the NH_3 generation rate is prominently higher than that of Ru system, due to Zr prefers binding N* adatoms rather than H* adatoms. DFT calculation proved that the Zr is effective at limiting the hydrogen evolution reaction. An energy diagram of this system is provided in Figure 15b.

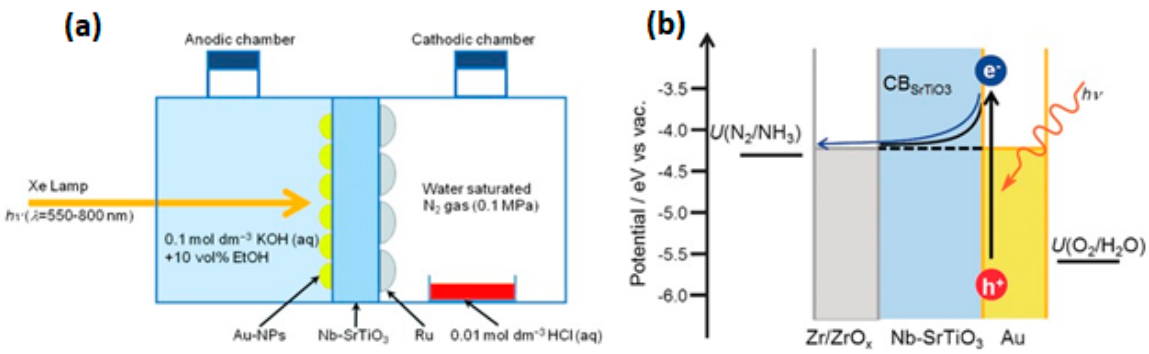

Figure 15. (**a**) A schematic illustration of the NH_3 synthesis device using a Nb-$SrTiO_3$ photoelectrode loaded with Au nanoparticles [80]; (**b**) Energy level diagram of the plasmon-induced NH_3 synthesis device [81]. (Reproduced with permission from the respective publishers).

Furthermore, Zheng, Terazono, and Tanuma attempted to synthesize ammonia at room temperature using Os-Au nanocomposite catalyst which was prepared by directly sputtered Os onto Au layer [79]. The generation of ammonia was observed under visible light irradiation between 550 and 650 nm, corresponding to the conversion rate of 0.003% at 550 nm. Originally, neither pure Au nor Os nanoparticle showed photoactivity in ammonia synthesis. Although pure Au nanoparticles exhibit LSPR effect of photon energy absorption to generate electron, but are unable to encourage the N_2 reduction reaction. Whereas, Os nanoparticle is active for N_2 fixation, but inactive in the visible light region. Therefore, the assembly of Au–Os nanocomposite motivates the photon energy resonance transfer from Au nanoparticles to Os layer (Figure 16a), enhancing NH_3 yield. By contrast, for the first time, Ali and his colleagues hypothesized that gold nanoparticles can serve as reduction cocatalyst [82]. In his work, solar-driven nanostructured plasmon enhanced black silicon photoelectrode produces ammonia yield of 320 mg m^{-2} in a day. The variety of controlled experiment confirm the roles of individual layers, which is described in Figure 16b. Gold nanoparticles (GNP) loaded black silicon (bSi) provide reduction active sites, receiving transferred electron form photon absorber bSi. While Cr layer acts as sacrificial hole sink where scavenge photogenerated holes by the oxidation of sulfite

ions. In results, the NH_3 production of the GNP/bSi/Cr cell increases to around two-folds that of the GNP/bSi and eight-folds that of pure bSi.

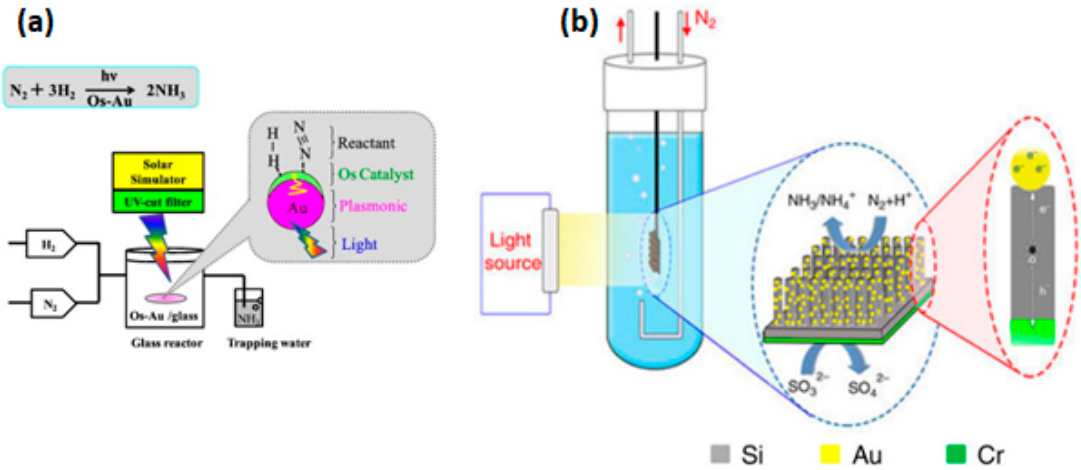

Figure 16. (**a**) A schematic illustration the mechanism of Au-Os nanocomposite for NH_3 photofixation [79]; (**b**) Schematic diagram of photochemical nitrogen reduction of Au/bSi/Cr [72]. (Reproduced with permission from the respective publishers).

5. Conclusions

Utilization of solar light for energy production and environmental protection is one of the most critical challenges in the near future for researchers and scientists. Photocatalyst based on semiconductors is an effective route to employ the plentiful energy from the sun. Unfortunately, industrial application of this strategy is still limited by ineffective light absorption and fast electrons-holes recombination process of photocatalyst semiconductor. Thus, the development of the active photocatalyst system is required. A variety of methods have been introduced to improve the photocatalytic efficiency, such as combining multicomponent semiconductor together, metal or non-metal doping, usage of cocatalyst, and plasmon-enhancement. The main purposes of these methods are to enhance the visible light absorption ability, to narrow band gap energy of semiconductor, to increase the charge separation, to decrease charge-recombination and to supply more active sites on the surface of the nanocomposite semiconductor.

Over the last decade, nitrogen photofixation has been attracted many interests for the synthesis of ammonia by nitrogen and water under solar irradiation. There are two main strategies for developing efficient photocatalyst of nitrogen reduction. Introduction of metal active sites or non-metal vacancies not only provide more active centers to absorb nitrogen, but also weaken and activate N-N triple bond. Whereas, noble metals, such as Pt, Ru, Pd, Rh loaded photocatalysts can act as electron acceptors, promoting charge carrier separation and suppressing electron hole recombination. In addition, loading gold nanoparticle induces LSPS effect, which can enhance visible light absorption effectively. In this review report, we have demonstrated the advantages and disadvantage of each group of active centers-based semiconductors. Understanding the strong points and drawbacks of these materials is a very important step to develop new effective photocatalyst for NH_3 evolution based on solar-driven nitrogen fixation.

Funding: This research was funded by MITACS, FQRNT and NSERC.

Acknowledgments: Authors gratefully acknowledge the funding support from the MITACS, FQRNT and NSERC.

Conflicts of Interest: Authors have no conflicts of interest to declare.

References

1. Service, R.F. New recipe produces ammonia from air, water, and sunlight. *Science* **2014**, *345*, 610. [CrossRef] [PubMed]
2. Licht, S.; Cui, B.; Wang, B.; Li, F.-F.; Lau, J.; Liu, S. Ammonia synthesis by N_2 and steam electrolysis in molten hydroxide suspensions of nanoscale Fe_2O_3. *Science* **2014**, *345*, 637–640. [CrossRef] [PubMed]
3. Linsebigler, A.L.; Lu, G.; Yates, J.T. Photocatalysis on TiO_2 Surfaces: Principles, Mechanisms, and Selected Results. *Chem. Rev.* **1995**, *95*, 735–758. [CrossRef]
4. Datta, R.S.; Ou, J.Z.; Mohiuddin, M.; Carey, B.J.; Zhang, B.Y.; Khan, H.; Syed, N.; Zavabeti, A.; Haque, F.; Daeneke, T.; et al. Two dimensional $PbMoO_4$: A photocatalytic material derived from a naturally non-layered crystal. *Nano Energy* **2018**, *49*, 237–246.
5. Daeneke, T.; Khoshmanesh, K.; Mahmood, N.; de Castro, I.A.; Esrafilzadeh, D.; Barrow, S.J.; Dickey, M.D.; Kalantar-zadeh, K. Liquid metals: Fundamentals and applications in chemistry. *Chem. Soc. Rev.* **2018**, *47*, 4073–4111.
6. Kisch, H. Semiconductor Photocatalysis-Mechanistic and Synthetic Aspects. *Angew. Chem. Int. Ed.* **2013**, *52*, 812–847. [CrossRef] [PubMed]
7. Furube, A.; Asahi, T.; Masuhara, H.; Yamashita, H.; Anpo, M. Charge Carrier Dynamics of Standard TiO_2 Catalysts Revealed by Femtosecond Diffuse Reflectance Spectroscopy. *J. Phys. Chem. B* **1999**, *103*, 3120–3127. [CrossRef]
8. Habisreutinger Severin, N.; Schmidt-Mende, L.; Stolarczyk Jacek, K. Photocatalytic Reduction of CO_2 on TiO2 and Other Semiconductors. *Angew. Chem. Int. Ed.* **2013**, *52*, 7372–7408. [CrossRef]
9. Li, X.; Yu, J.; Low, J.; Fang, Y.; Xiao, J.; Chen, X. Engineering heterogeneous semiconductors for solar water splitting. *J. Mater. Chem. A* **2015**, *3*, 2485–2534. [CrossRef]
10. Schiavello, M.; Augugliaro, V.; Palmisano, L. An experimental method for the determination of the photon flow reflected and absorbed by aqueous dispersions containing polycrystalline solids in heterogeneous photocatalysis. *J. Catal.* **1991**, *127*, 332–341. [CrossRef]
11. Kisch, H.; Bahnemann, D. Best Practice in Photocatalysis: Comparing Rates or Apparent Quantum Yields? *J. Phys. Chem. Lett.* **2015**, *6*, 1907–1910. [CrossRef] [PubMed]
12. Buriak, J.M.; Kamat, P.V.; Schanze, K.S. Best Practices for Reporting on Heterogeneous Photocatalysis. *ACS Appl. Mater. Interfaces* **2014**, *6*, 11815–11816. [CrossRef] [PubMed]
13. Khan, S.U.M.; Al-Shahry, M.; Ingler, W.B. Efficient Photochemical Water Splitting by a Chemically Modified n-TiO_2. *Science* **2002**, *297*, 2243–2245. [CrossRef]
14. Jing, D.; Guo, L. A Novel Method for the Preparation of a Highly Stable and Active CdS Photocatalyst with a Special Surface Nanostructure. *J. Phys. Chem. B* **2006**, *110*, 11139–11145. [CrossRef] [PubMed]
15. Cao, J.; Sun, J.Z.; Hong, J.; Li, H.Y.; Chen, H.Z.; Wang, M. Carbon Nanotube/CdS Core–Shell Nanowires Prepared by a Simple Room-Temperature Chemical Reduction Method. *Adv. Mater.* **2004**, *16*, 84–87. [CrossRef]
16. Wang, X.; Liu, G.; Lu, G.Q.; Cheng, H.-M. Stable photocatalytic hydrogen evolution from water over ZnO–CdS core–shell nanorods. *Int. J. Hydrog. Energy* **2010**, *35*, 8199–8205. [CrossRef]
17. Wang, X.; Liu, G.; Chen, Z.-G.; Li, F.; Wang, L.; Lu, G.Q.; Cheng, H.-M. Enhanced photocatalytic hydrogen evolution by prolonging the lifetime of carriers in ZnO/CdS heterostructures. *Chem. Commun.* **2009**, *23*, 3452–3454. [CrossRef]
18. Hou, J.; Wang, Z.; Kan, W.; Jiao, S.; Zhu, H.; Kumar, R.V. Efficient visible-light-driven photocatalytic hydrogen production using CdS@TaON core-shell composites coupled with graphene oxide nanosheets. *J. Mater. Chem.* **2012**, *22*, 7291–7299. [CrossRef]
19. Khan, S.U.M.; Majumder, S.A. Optimization of p-silicon surface by etching and electrodeposition of Pt and Ni for photosplitting of water. *Int. J. Hydrog. Energy* **1989**, *14*, 653–660. [CrossRef]
20. Akikusa, J.; Khan, S.U.M. Photoelectrolysis of water to hydrogen in p-SiC/Pt and p-SiC/ n-TiO_2 cells. *Int. J. Hydrog. Energy* **2002**, *27*, 863–870. [CrossRef]
21. Gurunathan, K. Photocatalytic hydrogen production using transition metal ions-doped γ-Bi_2O_3 semiconductor particles. *Int. J. Hydrog. Energy* **2004**, *29*, 933–940. [CrossRef]
22. Jang, J.S.; Yoon, K.Y.; Xiao, X.; Fan, F.-R.F.; Bard, A.J. Development of a Potential Fe_2O_3-Based Photocatalyst Thin Film for Water Oxidation by Scanning Electrochemical Microscopy: Effects of Ag$-Fe_2O_3$ Nanocomposite and Sn Doping. *Chem. Mater.* **2009**, *21*, 4803–4810. [CrossRef]
23. Jang, J.S.; Choi, S.H.; Kim, H.G.; Lee, J.S. Location and State of Pt in Platinized CdS/TiO_2 Photocatalysts for Hydrogen Production from Water under Visible Light. *J. Phys. Chem. C* **2008**, *112*, 17200–17205. [CrossRef]

24. Maeda, K.; Xiong, A.; Yoshinaga, T.; Ikeda, T.; Sakamoto, N.; Hisatomi, T.; Takashima, M.; Lu, D.; Kanehara, M.; Setoyama, T.; et al. Photocatalytic Overall Water Splitting Promoted by Two Different Cocatalysts for Hydrogen and Oxygen Evolution under Visible Light. *Angew. Chem. Int. Ed.* **2010**, *49*, 4096–4099. [CrossRef] [PubMed]
25. Clavero, C. Plasmon-induced hot-electron generation at nanoparticle/metal-oxide interfaces for photovoltaic and photocatalytic devices. *Nat. Photonics* **2014**, *8*, 95. [CrossRef]
26. Ma, X.-C.; Dai, Y.; Yu, L.; Huang, B.-B. Energy transfer in plasmonic photocatalytic composites. *Light Sci. Appl.* **2016**, *5*, e16017. [CrossRef]
27. Mubeen, S.; Hernandez-Sosa, G.; Moses, D.; Lee, J.; Moskovits, M. Plasmonic Photosensitization of a Wide Band Gap Semiconductor: Converting Plasmons to Charge Carriers. *Nano Lett.* **2011**, *11*, 5548–5552. [CrossRef]
28. Fan, W.; Leung, M. Recent Development of Plasmonic Resonance-Based Photocatalysis and Photovoltaics for Solar Utilization. *Molecules* **2016**, *21*, 180. [CrossRef]
29. Cushing, S.K.; Li, J.; Meng, F.; Senty, T.R.; Suri, S.; Zhi, M.; Li, M.; Bristow, A.D.; Wu, N. Photocatalytic Activity Enhanced by Plasmonic Resonant Energy Transfer from Metal to Semiconductor. *J. Am. Chem. Soc.* **2012**, *134*, 15033–15041. [CrossRef]
30. Fujishima, A.; Honda, K. Electrochemical Photolysis of Water at a Semiconductor Electrode. *Nature* **1972**, *238*, 37. [CrossRef]
31. Li, H.; Shang, J.; Ai, Z.; Zhang, L. Efficient Visible Light Nitrogen Fixation with BiOBr Nanosheets of Oxygen Vacancies on the Exposed {001} Facets. *J. Am. Chem. Soc.* **2015**, *137*, 6393–6399. [CrossRef] [PubMed]
32. Yuan, S.-J.; Chen, J.-J.; Lin, Z.-Q.; Li, W.-W.; Sheng, G.-P.; Yu, H.-Q. Nitrate formation from atmospheric nitrogen and oxygen photocatalysed by nano-sized titanium dioxide. *Nat. Commun.* **2013**, *4*, 2249. [CrossRef] [PubMed]
33. Bozso, F.; Ertl, G.; Grunze, M.; Weiss, M. Interaction of nitrogen with iron surfaces: I. Fe(100) and Fe(111). *J. Catal.* **1977**, *49*, 18–41. [CrossRef]
34. Tennakone, K.; Wickramanayake, S.; Fernando, C.A.N.; Ileperuma, O.A.; Punchihewa, S. Photocatalytic nitrogen reduction using visible light. *J. Chem. Soc. Chem. Commun.* **1987**, *14*, 1078–1080. [CrossRef]
35. Khader, M.M.; Lichtin, N.N.; Vurens, G.H.; Salmeron, M.; Somorjai, G.A. Photoassisted catalytic dissociation of water and reduction of nitrogen to ammonia on partially reduced ferric oxide. *Langmuir* **1987**, *3*, 303–304. [CrossRef]
36. Zhao, W.; Zhang, J.; Zhu, X.; Zhang, M.; Tang, J.; Tan, M.; Wang, Y. Enhanced nitrogen photofixation on Fe-doped TiO_2 with highly exposed (101) facets in the presence of ethanol as scavenger. *Appl. Catal. B Environ.* **2014**, *144*, 468–477. [CrossRef]
37. Soria, J.; Conesa, J.C.; Augugliaro, V.; Palmisano, L.; Schiavello, M.; Sclafani, A. Dinitrogen photoreduction to ammonia over titanium dioxide powders doped with ferric ions. *J. Phys. Chem.* **1991**, *95*, 274–282. [CrossRef]
38. Rusina, O.; Linnik, O.; Eremenko, A.; Kisch, H. Nitrogen Photofixation on Nanostructured Iron Titanate Films. *Chem. A Eur. J.* **2003**, *9*, 561–565. [CrossRef] [PubMed]
39. Linnik, O.; Kisch, H. On the mechanism of nitrogen photofixation at nanostructured iron titanate films. *Photochem. Photobiol. Sci.* **2006**, *5*, 938–942. [CrossRef]
40. Lashgari, M.; Zeinalkhani, P. Photocatalytic N_2 conversion to ammonia using efficient nanostructured solar-energy-materials in aqueous media: A novel hydrogenation strategy and basic understanding of the phenomenon. *Appl. Catal. A General* **2017**, *529*, 91–97. [CrossRef]
41. Hu, S.; Chen, X.; Li, Q.; Li, F.; Fan, Z.; Wang, H.; Wang, Y.; Zheng, B.; Wu, G. Fe^{3+} doping promoted N_2 photofixation ability of honeycombed graphitic carbon nitride: The experimental and density functional theory simulation analysis. *Appl. Catal. B Environ.* **2017**, *201*, 58–69. [CrossRef]
42. Schrauzer, G.N.; Guth, T.D. Photocatalytic reactions. 1. Photolysis of water and photoreduction of nitrogen on titanium dioxide. *J. Am. Chem. Soc.* **1977**, *99*, 7189–7193. [CrossRef]
43. Tennakone, K.; Bandara, J.M.S.; Thaminimulla, C.T.K.; Jayatilake, W.D.W.; Ketipearachchi, U.S.; Ileperuma, O.A.; Priyadarshana, M.K.A. Photoreduction of dinitrogen to ammonia by ultrafine particles of iron hydroxide oxide (Fe(O)OH) formed by photohydrolysis of iron(II) bicarbonate. *Langmuir* **1991**, *7*, 2166–2168. [CrossRef]
44. Lu, Y.; Yang, Y.; Zhang, T.; Ge, Z.; Chang, H.; Xiao, P.; Xie, Y.; Hua, L.; Li, Q.; Li, H.; et al. Photoprompted Hot Electrons from Bulk Cross-Linked Graphene Materials and Their Efficient Catalysis for Atmospheric Ammonia Synthesis. *ACS Nano* **2016**, *10*, 10507–10515. [CrossRef] [PubMed]

45. Tennakone, K.; Fernando, C.A.N.; Wickramanayake, S.; Damayanthi, M.W.P.; Silva, L.H.K.; Wijeratne, W.; Illeperuma, O.A.; Punchihewa, S. Photocatalytic reduction of nitrogen to ammonia with coprecipitated Fe(III) and Ti(IV) hydrous oxides. *Sol. Energy Mater.* **1988**, *17*, 47–53. [CrossRef]
46. Ileperuma, O.A.; Kiridena, W.C.B.; Dissanayake, W.D.D. Photoreduction of nitrogen and water on montmorillonite clays loaded with hydrous ferric oxide. *J. Photochem. Photobiol. A Chem.* **1991**, *59*, 191–197. [CrossRef]
47. Baumann, R.; Stumpf, R.; Davis, W.M.; Liang, L.-C.; Schrock, R.R. Titanium and Zirconium Complexes That Contain the Tridentate Diamido Ligands [(i-PrN-o-C6H4)2O]2-([i-PrNON]2-) and [(C6H11N-o-C6H4)2O]2-([CyNON]2-). *J. Am. Chem. Soc.* **1999**, *121*, 7822–7836. [CrossRef]
48. Van Tamelen, E.E.; Fechter, R.B.; Schneller, S.W. Conversion of molecular nitrogen to hydrazine. *J. Am. Chem. Soc.* **1969**, *91*, 7196. [CrossRef]
49. Hirakawa, H.; Hashimoto, M.; Shiraishi, Y.; Hirai, T. Photocatalytic Conversion of Nitrogen to Ammonia with Water on Surface Oxygen Vacancies of Titanium Dioxide. *J. Am. Chem. Soc.* **2017**, *139*, 10929–10936. [CrossRef]
50. Sun, S.; Li, X.; Wang, W.; Zhang, L.; Sun, X. Photocatalytic robust solar energy reduction of dinitrogen to ammonia on ultrathin MoS_2. *Appl. Catal. B Environ.* **2017**, *200*, 323–329. [CrossRef]
51. Banerjee, A.; Yuhas, B.D.; Margulies, E.A.; Zhang, Y.; Shim, Y.; Wasielewski, M.R.; Kanatzidis, M.G. Photochemical Nitrogen Conversion to Ammonia in Ambient Conditions with FeMoS-Chalcogels. *J. Am. Chem. Soc.* **2015**, *137*, 2030–2034. [CrossRef] [PubMed]
52. Liu, J.; Kelley, M.S.; Wu, W.; Banerjee, A.; Douvalis, A.P.; Wu, J.; Zhang, Y.; Schatz, G.C.; Kanatzidis, M.G. Nitrogenase-mimic iron-containing chalcogels for photochemical reduction of dinitrogen to ammonia. *Proc. Natl. Acad. Sci. USA* **2016**, *113*, 5530–5535. [CrossRef] [PubMed]
53. Hoffman, B.M.; Lukoyanov, D.; Yang, Z.-Y.; Dean, D.R.; Seefeldt, L.C. Mechanism of Nitrogen Fixation by Nitrogenase: The Next Stage. *Chem. Rev.* **2014**, *114*, 4041–4062. [CrossRef] [PubMed]
54. Ye, L.; Han, C.; Ma, Z.; Leng, Y.; Li, J.; Ji, X.; Bi, D.; Xie, H.; Huang, Z. Ni_2P loading on Cd0.5Zn0.5S solid solution for exceptional photocatalytic nitrogen fixation under visible light. *Chem. Eng. J.* **2017**, *307*, 311–318. [CrossRef]
55. Wang, S.; Hai, X.; Ding, X.; Chang, K.; Xiang, Y.; Meng, X.; Yang, Z.; Chen, H.; Ye, J. Light-Switchable Oxygen Vacancies in Ultrafine Bi5O7Br Nanotubes for Boosting Solar-Driven Nitrogen Fixation in Pure Water. *Adv. Mater.* **2017**, *29*, 1701774. [CrossRef]
56. Li, C.; Wang, T.; Zhao, Z.J.; Yang, W.; Li, J.F.; Li, A.; Yang, Z.; Ozin Geoffrey, A.; Gong, J. Promoted Fixation of Molecular Nitrogen with Surface Oxygen Vacancies on Plasmon-Enhanced TiO_2 Photoelectrodes. *Angew. Chem. Int. Ed.* **2018**, *57*, 5278–5282. [CrossRef] [PubMed]
57. Sun, S.; An, Q.; Wang, W.; Zhang, L.; Liu, J.; Goddard Iii, W.A. Efficient photocatalytic reduction of dinitrogen to ammonia on bismuth monoxide quantum dots. *J. Mater. Chem. A* **2017**, *5*, 201–209. [CrossRef]
58. Zhang, X.; Zhang, G.; Zou, J. Nitrogen reduction utilizing solvated electrons produced by thermal excitation of trapped electrons in reduced titanium oxide. *New J. Chem.* **2018**, *42*, 6084–6090. [CrossRef]
59. Li, H.; Shang, J.; Shi, J.; Zhao, K.; Zhang, L. Facet-dependent solar ammonia synthesis of BiOCl nanosheets via a proton-assisted electron transfer pathway. *Nanoscale* **2016**, *8*, 1986–1993. [CrossRef]
60. Bai, Y.; Ye, L.; Chen, T.; Wang, L.; Shi, X.; Zhang, X.; Chen, D. Facet-Dependent Photocatalytic N_2 Fixation of Bismuth-Rich Bi_5O_7I Nanosheets. *ACS Appl. Mater. Interfaces* **2016**, *8*, 27661–27668. [CrossRef]
61. Zhao, Y.; Zhao, Y.; Waterhouse, G.I.N.; Zheng, L.; Cao, X.; Teng, F.; Wu, L.-Z.; Tung, C.-H.; O'Hare, D.; Zhang, T. Layered-Double-Hydroxide Nanosheets as Efficient Visible-Light-Driven Photocatalysts for Dinitrogen Fixation. *Adv. Mater.* **2017**, *29*, 1703828. [CrossRef] [PubMed]
62. Hao, Y.; Dong, X.; Zhai, S.; Ma, H.; Wang, X.; Zhang, X. Hydrogenated Bismuth Molybdate Nanoframe for Efficient Sunlight-Driven Nitrogen Fixation from Air. *Chem. A Eur. J.* **2016**, *22*, 18722–18728. [CrossRef] [PubMed]
63. Comer, B.M.; Medford, A.J. Analysis of Photocatalytic Nitrogen Fixation on Rutile TiO_2(110). *ACS Sustain. Chem. Eng.* **2018**, *6*, 4648–4660. [CrossRef]
64. Li, J.; Li, H.; Zhan, G.; Zhang, L. Solar Water Splitting and Nitrogen Fixation with Layered Bismuth Oxyhalides. *Acc. Chem. Res.* **2017**, *50*, 112–121. [CrossRef] [PubMed]
65. Li, H.; Li, J.; Ai, Z.; Jia, F.; Zhang, L. Oxygen Vacancy-Mediated Photocatalysis of BiOCl: Reactivity, Selectivity, and Perspectives. *Angew. Chem. Int. Ed.* **2017**, *57*, 122–138. [CrossRef] [PubMed]

66. Dong, G.; Ho, W.; Wang, C. Selective photocatalytic N2 fixation dependent on g-C3N4 induced by nitrogen vacancies. *J. Mater. Chem. A* **2015**, *3*, 23435–23441. [CrossRef]
67. Li, S.; Chen, X.; Hu, S.; Li, Q.; Bai, J.; Wang, F. Infrared ray assisted microwave synthesis: A convenient method for large-scale production of graphitic carbon nitride with outstanding nitrogen photofixation ability. *RSC Adv.* **2016**, *6*, 45931–45937. [CrossRef]
68. Ma, H.; Shi, Z.; Li, Q.; Li, S. Preparation of graphitic carbon nitride with large specific surface area and outstanding N_2 photofixation ability via a dissolve-regrowth process. *J. Phys. Chem. Solids* **2016**, *99*, 51–58. [CrossRef]
69. Zhou, N.; Qiu, P.; Chen, H.; Jiang, F. KOH etching graphitic carbon nitride for simulated sunlight photocatalytic nitrogen fixation with cyano groups as defects. *J. Taiwan Inst. Chem. Eng.* **2018**, *83*, 99–106. [CrossRef]
70. Hu, S.; Chen, X.; Li, Q.; Zhao, Y.; Mao, W. Effect of sulfur vacancies on the nitrogen photofixation performance of ternary metal sulfide photocatalysts. *Catal. Sci. Technol.* **2016**, *6*, 5884–5890. [CrossRef]
71. Zhang, Q.; Hu, S.; Fan, Z.; Liu, D.; Zhao, Y.; Ma, H.; Li, F. Preparation of g-C3N4/ZnMoCdS hybrid heterojunction catalyst with outstanding nitrogen photofixation performance under visible light via hydrothermal post-treatment. *Dalton Trans.* **2016**, *45*, 3497–3505. [CrossRef] [PubMed]
72. Cao, Y.; Hu, S.; Li, F.; Fan, Z.; Bai, J.; Lu, G.; Wang, Q. Photofixation of atmospheric nitrogen to ammonia with a novel ternary metal sulfide catalyst under visible light. *RSC Adv.* **2016**, *6*, 49862–49867. [CrossRef]
73. Hu, S.; Li, Y.; Li, F.; Fan, Z.; Ma, H.; Li, W.; Kang, X. Construction of g-C3N4/Zn0.11Sn0.12Cd0.88S1.12 Hybrid Heterojunction Catalyst with Outstanding Nitrogen Photofixation Performance Induced by Sulfur Vacancies. *ACS Sustain. Chem. Eng.* **2016**, *4*, 2269–2278. [CrossRef]
74. Miyama, H.; Fujii, N.; Nagae, Y. Heterogeneous photocatalytic synthesis of ammonia from water and nitrogen. *Chem. Phys. Lett.* **1980**, *74*, 523–524. [CrossRef]
75. Khan Mirza, M.T.; Bhardwaj Ramesh, C.; Bhardwaj, C. Catalytic Fixation of Nitrogen by the Photocatalytic CdS/Pt/RuO2 Particulate System in the Presence of Aqueous [Ru(Hedta)N2]⊖ Complex. *Angew. Chem. Int. Ed. Engl.* **1988**, *27*, 923–925. [CrossRef]
76. Ranjit, K.T.; Varadarajan, T.K.; Viswanathan, B. Photocatalytic reduction of dinitrogen to ammonia over noble-metal-loaded TiO_2. *J. Photochem. Photobiol. A Chem.* **1996**, *96*, 181–185. [CrossRef]
77. Rao, N.N.; Dube, S.; Manjubala; Natarajan, P. Photocatalytic reduction of nitrogen over (Fe, Ru or Os) /TiO_2 catalysts. *Appl. Catal. B Environ.* **1994**, *5*, 33–42. [CrossRef]
78. Medford, A.J.; Hatzell, M.C. Photon-Driven Nitrogen Fixation: Current Progress, Thermodynamic Considerations, and Future Outlook. *ACS Catal.* **2017**, *7*, 2624–2643. [CrossRef]
79. Zeng, H.; Terazono, S.; Tanuma, T. A novel catalyst for ammonia synthesis at ambient temperature and pressure: Visible light responsive photocatalyst using localized surface plasmon resonance. *Catal. Commun.* **2015**, *59*, 40–44. [CrossRef]
80. Oshikiri, T.; Ueno, K.; Misawa, H. Plasmon-Induced Ammonia Synthesis through Nitrogen Photofixation with Visible Light Irradiation. *Angew. Chem. Int. Ed.* **2014**, *53*, 9802–9805. [CrossRef]
81. Oshikiri, T.; Ueno, K.; Misawa, H. Selective Dinitrogen Conversion to Ammonia Using Water and Visible Light through Plasmon-induced Charge Separation. *Angew. Chem.* **2016**, *128*, 4010–4014. [CrossRef]
82. Ali, M.; Zhou, F.; Chen, K.; Kotzur, C.; Xiao, C.; Bourgeois, L.; Zhang, X.; MacFarlane, D.R. Nanostructured photoelectrochemical solar cell for nitrogen reduction using plasmon-enhanced black silicon. *Na. Commun.* **2016**, *7*, 11335. [CrossRef] [PubMed]
83. Ueno, K.; Oshikiri, T.; Shi, X.; Zhong, Y.; Misawa, H. Plasmon-induced artificial photosynthesis. *Interface Focus* **2015**, *5*, 20140082. [CrossRef] [PubMed]